CHARACTERISTICS AND SOURCE MODELING OF BROADBAND SEISMIC SIGNALS ASSOCIATED WITH THE HYDROTHERMAL SYSTEM AT SATSUMA-IWOJIMA VOLCANO, JAPAN

Takao Ohminato

Earthquake Research Institute, Tokyo University

1-1-1 Yayoi, Bunkyo-ku, Tokyo, 113-0032 JAPAN

Phone: +81-3-5841-5810, Fax: +81-3-3812-6979 , E-mail: takao@eri.u-tokyo.ac.jp

Abstract

The broadband seismic data observed at Satsuma-Iwojima volcanic island in southwestern Japan show a wide variety of interesting features. One of them is the periodic and frequency-dependent amplitude modulation of volcanic tremors. Another interesting feature is the occurrence of very long-period (VLP) seismic pulses synchronized with the tremor amplitude modulation. Both the tremor amplitude modulation and the VLP pulses have fairly regular intervals of 46-50 min, suggesting a spatially fixed, non-destructive repetitive source. We performed waveform inversions to reveal the source mechanism of the VLP pulses, assuming a point source embedded in a medium that realistically represented the topography of the island. Numerical tests showed that the Green's functions used in the inversion were significantly affected by the topography. The observed VLP pulses were well explained by the rapid expansion of an inclined crack 100 m beneath the floor of the summit crater, which had a seismic moment of 3×10^{10}Nm. Both the characteristic amplitude modulation and the VLP pulses are explained systematically by a model consisting of a water-filled crack and a network of gas paths. The water-filled crack was heated above the boiling temperature of the water in it. A sudden break of the unstable superheated state caused sudden vaporization and a pressure increase, which was observed as the VLP pulse. The network of gas paths consisted of swollen portions and constricted portions, which worked as tremor generators when vapor from the water-filled crack passed through.

Keywords: volcanic tremor; regular amplitude modulation; Satsuma-Iwojima; waveform analysis

1. Introduction

Satsuma-Iwojima is a volcanic island located on the northwestern rim of the submarine Kikai Caldera (Fig.1 a), whose last eruption occurred about 6300 years ago with an emission of more than 170 km^3 of tephra (Machida and Arai, 1992). The western part of Satsuma-Iwojima is composed of andesitic to rhyolitic lava and the eastern half of the island is occupied by a rhyolitic cone called Iwodake, which has an active crater at its summit of 400 m in diameter. At the bottom of the crater, there is a gradually expanding fumarolic vent, which continuously and steadily emits high-temperature volcanic gas at nearly 900°C (Shinohara et al., 2002). In April 1997, the vent was roughly 30 m in diameter. By November 1999, the diameter had increased to 40 m (Shinohara et al., 2002). In addition to the central vent, there are many small, active fumarolic vents in and around the summit area of Iwodake. Volcanic gas emitted from the summit vent and fumaroles is mainly composed of H_2O, HCl and SO_2. The current emission rates of H_2O and SO_2 are estimated at 1.6×10^4t/day and 5.5×10^2 t/day, respectively (Kazahaya et al., 2002). The volcanic gas emission from the summit crater is thought to have continued for over 800 years (Yoshida and Ozawa, 1981).

From April 17 to 21, 1997, we installed a seismic network composed of 5 short period sensors and 3 broadband sensors around Iwodake, from the bottom to the top, as shown in Fig.1. This was the first broadband seismic observation conducted at Satsuma-Iwojima. The broadband seismic signals recorded by the network exhibit a wide variety of interesting features. One of the most interesting is a periodic amplitude modulation of volcanic tremor with a characteristic envelope. Another interesting feature is the occurrence of very long-period (VLP) seismic pulses,

which are perfectly synchronized with the tremor amplitude modulation (Ohminato and Ereditato, 1997).

There have been various types of periodic seismic signals observed in and around volcanoes worldwide. Periodicities in volcanic tremor are often manifested as sharp spectral peaks in the frequency domain. Such spectral peaks of volcanic tremor are widely observed at many volcanoes with a typical frequency range of 0.5-5Hz (e.g., Kamo et al., 1977; Benoit and McNutt, 1997). Some of the periodicities of seismic signals are seen more clearly in the time domain than in the frequency domain. An example of periodicity clearly seen in the time domain is the quasi-periodical or sporadic excitations of a series of volcanic tremors or the activation of swarms (e.g., Fig.1K in McNutt, 1996). Another example of time domain periodicity is the *saw-toothed* signal observed at Kilauea volcano, Hawaii, during the volcanic crisis on February 1, 1996. In that signal, the intervals between saw teeth were 2 to 3min (Ohminato et al., 1998). Periodic seismic signals are observed not only in volcanic areas, but also in geothermal ones. The periodic seismic signals observed at Old Faithful Geyser, Wyoming, are presumably independent of either magma transportation or volcanic gas flow. Typical eruptions of the Geyser last 1.5-5.5min, with intervals ranging from 30 to 100 min (Kieffer, 1984). The source of seismic signals at Old Faithful Geyser is most likely caused by individual bubble collapses, occurring at the top of the super-heated water column. The observed change in the event rate is attributed to widening and narrowing of the water filled conduit (Kedar 1996).

The periodic signals observed in volcanic or geothermal areas originate from various types of physical processes. Some of the source processes are associated with magma transportation and others are associated with the boiling of ground water, although their frequency ranges are not

necessarily separated from each other. Thus, determining the locations of dominant frequency peaks does not provide sufficient information to specify the physical processes behind periodic signals. In the periodic seismic signals observed at Satsuma-Iwojima during our observation, however, not only the frequency peaks but also frequency-dependent amplitude modulation was observed. Using these two different types of information, we are able to discuss the source physics in much greater depth than when using only one type of information.

In this paper, we perform not only a spectral analysis on the volcanic tremor to investigate the physical processes behind it, but an investigation of the source mechanism of the highly periodic VLP pulses which was conducted by applying a waveform inversion technique to the broadband seismic data. Waveform inversion of the source mechanisms and source time functions using broadband seismic data obtained in and around active volcanoes has become one of the standard techniques in the field of volcanic seismology (e.g., Uhira and Takeo, 1994; Ohminato et al., 1998; Nishimura et al., 2000; Legrand et al., 2000; Cruz-Atienza et al., 2001, Nakano et al., 2003). However, the results of waveform inversions in previous studies may have been distorted due to the usage of relatively simple Green's functions computed without considering the steep volcanic topography, which may significantly affect the waveforms observed. Ohminato and Chouet (1997) qualitatively noted the effect of steep topography on seismic waveforms in the lower frequency range based on the results of numerical simulations. The importance of topographic effects in the frequency range higher than 1Hz was shown by Almendrus et al. (2001) in the analysis of seismic array data obtained at Kilauea, Hawaii. Chouet et al. (2003) analyzed broadband seismic data associated with eruptions at a 2-30s period range at Stromboli volcano, Italy, taking into account the effect of topography. Chouet et al. (2005) applied the same technique to the VLP

signals accompanying vulcanian activities at Popocatepetl volcano, Mexico. To analyze the VLP signals observed at Satsuma-Iwojima, we used Green's functions computed by using a finite difference method (FDM) in which arbitrary structure and topography can be included (Ohminato and Chouet, 1997).

In the following sections, we begin with a brief description of the data acquisition. We then proceed to a detailed description of the characteristics of the observed seismic signals, including the results of frequency analyses of volcanic tremors whose amplitude is modulated at quasi-regular intervals. We then move on to an analysis of waveform inversions of the low-pass filtered broadband data. Finally, we discuss possible models that can explain both the modulating tremors and VLP signals. We use the term *very long period* (VLP) for signals whose characteristic period is above 5 sec, following the classification of period range proposed by Chouet (1996).

2. Data and characteristics of broadband data

We conducted broadband seismic observations at Satsuma-Iwojima from April 17 to 21, 1997. Due to high ground temperature and corrosive volcanic gases, only very limited areas were suitable for seismic sensor installation in the summit area of Iwodake. To avoid erosion by volcanic gas, all the sensors and data loggers were sealed in plastic bags. We installed 5 Mark Products L4 vertical sensors and 3 Guralp CMG-40T 3-component sensors (Fig.1b). The characteristic periods are 1 sec for the former and 30 sec for the latter. The velocity outputs were recorded using Data Mark LS8000SH portable recorders equipped with 20 MB of storage. The sampling rate was 100 Hz. The internal clock was synchronized with GPS timing every 2-3 hours. Due to the storage

limitations of the data loggers, and to avoid man-made noise from nearby mines, the period of continuous recording for the three component sensors (CMG-40T) was restricted to the hours of 10pm to 8am the following morning. The continuous recordings at the single component stations lasted three times longer than at the three component stations. In addition to 100 Hz recordings, a recording at 200 Hz at station ST1 was also performed on April 18th. This 200 Hz recording made it possible to see characteristic features of volcanic tremors in the frequency range higher than 40 Hz. The recording system SAM manufactured by Guralp Co. recorded 10 hours of 200 Hz seismograms at ST1 before the corrosive gas damaged the recorder.

2.1. Tremor amplitude modulation and VLP pulses

We here summarize the features of the seismic records reported by Ohminato and Ereditato (1997). One of the most interesting features is regular amplitude modulation of volcanic tremor (Fig.2, top). The amplitude modulation is particularly clear at ST3, possibly due to its close proximity to the source. Another significant feature is the presence of VLP pulses that can best be recognized in the low-pass filtered traces at 0.2Hz recorded by the broadband sensor at ST1 (Fig.2, bottom). It is difficult to recognize VLP pulses in short period seismograms without using the broadband record as a timing reference. The intervals of pulses are fairly regular (Fig.3). Most of the pulse intervals fall into the period range of 46-50 min. No interval shorter than 38 min or longer than 78 min was found during the observation period.

As we observed the tremor record in more detail, we saw that the periodical amplitude modulation was frequency dependent. Fig.4a shows the vertical component of a seismic trace

observed at ST1 on April 18, 1997. From the top to the bottom, the figure shows an unfiltered trace, an envelope of the top trace, a high-pass filtered trace at 40 Hz, and a low-pass filtered trace at 0.2Hz. These four panels clearly show frequency-dependent characteristic features of the amplitude modulation. The envelope in the second panel of Fig.4a most clearly shows the characteristic property of the amplitude modulation in the intermediate frequency range (1-40Hz, the frequency range we call an IMF-range in this paper). In this frequency range, the modulation is composed of two stages, an amplitude-increasing stage and a decreasing stage. Hereafter, we call these two stages the Inc-Stage and Dec-Stage, respectively. Inc-Stages last for about 10-15 minutes, and Dec-Stages for about 30-35 minutes. In an Inc-Stage (an amplitude increasing stage), the shape of the envelope is always an upward convex, while in a Dec-Stage (an amplitude decreasing stage), the shape of the envelope is always concave. In the IMF-range, the amplitude modulation is composed of the repetition of these two stages occurring alternately.

In the frequency range higher than 40Hz (which we call the HF-range in this paper), the amplitude modulation is composed of four stages: (1) a stage of abrupt onset, (2) a stage of gradual amplitude decay, (3) a stage of rapid amplitude decay, and (4) a stage of low amplitude as shown in the third panel from the top of Fig.4a. The abrupt onset of the tremor in the HF-range is perfectly synchronized with the time when the envelope of the tremor in the IMF-range changes from its concave stage (Dec-Stage) to its upward convex stage (Inc-Stage). The end of the stage of rapid amplitude decrease in the HF-range coincides with the timing when the tremor envelope in the IMF-range changes from an Inc-Stage to a Dec-Stage. These characteristics are summarized in the schematic diagram shown in Fig.4b.

As shown in the bottom panel of Fig.4a, pulse-shaped signals are clearly seen in the

frequency range below 0.2Hz (which we call the LF-range in this paper). The peak frequencies of these signals are around 0.1 Hz. We will call these signals VLP pulses hereafter. Each VLP pulse is perfectly synchronized with the abrupt onset of the HF tremor. This timing coincides with the beginning of an Inc-Stage of the tremor envelope in the IMF-range (see the second panel in Fig.4b).

In Fig.4b, the frequency-dependent characteristics are schematically summarized. The tremor envelope at the IMF-range is composed of alternate occurrences of Inc-Stages and Dec-Stages. The HF tremor has 4 stages ((1), (2), (3), and (4) in Fig.4b). An occurrence of each VLP signal is perfectly synchronized with the abrupt onset of tremor in the HF-range and with the beginning of an Inc-Stage in the IMF-range. The synchronicities between features in different frequency ranges are also clearly seen in spectrograms. The synchronicity between the HF-range and the IMF-range is shown in Fig.5.

2.2.The features seen in the spectrograms

Figs.6 and 7 show spectrograms of the 3-hour records that were obtained from 15:21 to 18:21 on April 18, 1997 at 4 summit stations, ST1, ST2, ST3, and ST4. The amplitude modulation occurred over a wide frequency range. The most important feature of these spectrograms is the existence of banded structures. Although the positions of the horizontal spectral bands are stable at each station, the frequencies corresponding to these horizontal spectral bands differ from station to station.

In active volcanoes or geothermal areas, distinct spectral peaks in seismic records are often observed. The appearances of spectral peaks differ from place to place and event to event. In

some cases, peak locations shift with time. In other cases, peak locations are stable for a long period of time. An example of time-variable peak locations is the behavior of spectral peaks of volcanic tremor observed at Arenal Volcano, Costa Rica (Benoit and McNutt, 1997). The spectral peaks observed at Arenal Volcano shift systematically with time, and the shift is interpreted as a change in the resonating frequency of magma-filled conduit due to a change in the gas content of the magma. Similar types of peak shift in spectrograms have been observed worldwide; Sakurajima, Japan (Kamo et al., 1977), Langila, Papua New Guinea (Mori et al., 1989), Semeru, Indonesia (Schlindwein et al., 1995), Erebus in Antactica (Rowe et al., 2000), and Montserrat (Neuberg et al., 2000; Powell and Neuberg, 2003). Generally speaking, variable spectral peaks are often attributed to a source effect. In contrast, time independent spectral peaks are also observed in volcanic or geothermal areas and are often attributed to a site effect. The spectral feature of the tremor observed at Old Faithful Geyser is an example of a case in which the spectral peaks do not change significantly with time. The stable behavior of spectral peaks observed at Old Faithful Geyser has been interpreted as a site effect (Kedar et al., 1996).

Many of the spectral peaks observed at Satsuma-Iwojima do not change its position with time, suggesting the existence of a site effect. However, some of these peaks are the same for all 4 summit stations, as shown in the stacked spectra in Fig.8. Are these common peaks explained solely by the site effect? The spectra of the volcanic tremor are shown on the left-hand side, and the spectra of a non-volcanic (tectonic) earthquake on the right-hand side. When a volcanic tremor (Fig.8a) occurs, both common spectral peaks (e.g., a peak at around 20 Hz) and spectral peaks that are not common to all 4 summit stations are seen. By contrast, there is no spectral peak common to all 4 stations when there is a tectonic event (Fig.8b). Since the common peaks observed when

volcanic tremor occurs do not appear each time a tectonic event occurs, these common spectral peaks strongly suggest the existence of source effects. In addition, tremor amplitude modulations with high periodicity are found at all 4 summit stations. This observation also suggests a source effect. Thus, our observations strongly suggest the coexistence of path effects and source effects in the characteristic tremor spectrum.

2.3. Polarization of VLP pulses

At the stations (ST1, ST2, ST3 and ST4) in the summit area of Iwodake, VLP pulses are clearly seen. However, the signal-to-noise ratio is low at stations at the flank and at the bottom of Iwodake (ST5, ST6, ST7 and ST8). Since most of the VLP pulses observed at ST1 have almost identical shapes, we can assume that the source locations and the source mechanisms are almost identical for all of the identical pulses. In order to improve the signal-to-noise ratio, we conducted stacking of waveforms using the onset time of each pulse at ST1 as a reference of timing under the common source assumption. As shown in Fig.9, an application of stacking dramatically improved the signal-to-noise ratio at all 8 stations, and made it possible to see the waveforms in detail. The success in the waveform stacking also justified the assumption that the source mechanisms are almost identical for all of the VLP pulses.

The vertical component of the stacked velocity at ST1 reveals the interesting feature of the VLP signal much more clearly (Fig.9a). The stacked VLP signal in the velocity is composed of two peaks with durations of 1 s and 2-4 s, respectively. The total duration of the stacked VLP pulse is roughly 3-4 s. A downward initial motion is clearly seen in the stacked signal of ST8 (Fig.9b).

The downward initial motion observed at a seismic station is often interpreted as a dilatational source mechanism when it is presumed that the source elevation is lower than the station elevation. In a volcanic environment, however, the source elevation can be higher than the station elevation, and thus the observed downward onset does not necessarily mean a dilatational source. If a source is shallower than the station, then the initial onset at the station can be downward even if the source mechanism is compressional. The vertical components of all the summit stations except for ST4 are characterized by upward initial motions. However, the vertical components of the three stations at the foot (ST5, ST7 and ST8) and the one station at the flank (ST6) have downward initial motions. These observations suggest that the source mechanism consists mainly of volumetric expansion, and that the source depth from the surface falls between the summit and bottom of the edifice of Iwodake.

In Fig.10, the particle velocities of the stacked waveforms at the three component stations, ST1, ST6, and ST7, are shown in the plan and sectional views of a schematic diagram of Iwodake. The particle velocity of the VLP pulse at ST1 has high rectilinearity, suggesting that the seismic signal is mainly composed of P waves radiated from a volumetric expansion source. The initial portion of the particle velocity at ST1 points almost eastward and slightly upwards with a shallow angle from beneath the summit crater. However, the initial directions of the particle velocities observed at ST6 and ST7 are not as clear as those observed at ST1. Probably due to the relatively long source-receiver distance of ST6 and ST7, only the very beginnings of the stacked signals exhibit rectilinearity. The particle velocity at ST6 exhibits an outward and slightly downward motion. At ST7, located at the base of Iwodake, the particle velocity points downwards and outwards from the summit. These particle velocities observed at ST1, ST6 and ST7 give us a rough

estimate of the source location. A fumarolic vent with a diameter of 30m at the center of the summit crater of Iwodake is located approximately 400m west of ST1, and emits high temperature volcanic gases continuously. If we assume that the source of the VLP pulses is located beneath the center of the summit crater, the source depth is estimated to be approximately 40 m beneath the bottom of the summit crater.

Particle velocity analyses of VLP for estimating source location have been widely adopted at Stromboli (Neuberg and Luckett, 1996; Chouet et al., 1999), Aso (Kawakatsu et al., 2000), Usu (Yamamoto et al., 2002), Erebus (Rowe et al., 1998, 2000; Aster et al., 2003), and other volcanoes. We used the waveform semblance method proposed by Kawakatsu et al. (2000), which uses not only the arrival time differences, but also the rectilinearity of the particle motions. This method is an extension of the original semblance method of Neidel and Tarner (1971). Neuberg and Luckett (1996) and Rowe et al. (2000) suggest that particle motions do not necessarily point to the source location due to the existence of the free surface boundary. However, Ohminato et al. (1998) show that the source location obtained by the particle velocity analysis method is in close vicinity to the source location derived from a waveform match. Almendros et al. (2003) test the effect of the flat free surface to the apparent incident angle by generating synthetic seismograms with periods of 2 sec and 20 sec. According to their test, the particle motions tend to define a diffuse region shallower than the actual source when the wavelength is short, while when the wavelength is long, the particle motions point to the correct source location. Their test results suggest that the topographic effect is less sensitive to a longer period.

In our case, the dominant period of VLP pulses were roughly 10sec, and thus the source depth estimated by the particle velocity analyses would be shallower than the actual depth. In fact,

the estimated depth of 40m is shallower than the depth of 100m that was obtained by the waveform matching described in the next section. The location indicated by the particle velocity analysis will be used as an initial guess around which a grid search is conducted for an exact source location.

As the initial source location has been estimated, we will now move on to the next step of waveform analysis. In the following sections, we perform waveform inversions using the source location estimated here by the particle velocity analysis as an initial source location. We then conduct a grid search to find the best-fit solution. Note here that there is the limitation originated from the instrumental passband. It is possible that the apparent dilatational onset of the signals may simply be a manifestation of this limitation (e.g., Rowe et al., 1998; Neuberg et al., 1994). Our observation was totally blind to physical processes with a time constant longer than 30s. The result of the waveform analysis explained below and the following discussion are based on this limited passband.

3. Inversion method

In conducting waveform inversions, we need to compute Green's functions, which represent the response of a medium to a given impulsive force. Omitting the topographic effect on Green's functions may be justified as long as the characteristic length of topography is not comparable to the dominant wavelength of the seismic signals under consideration. In the case of the VLP signals observed at Iwodake, the dominant frequency is below 0.2Hz, and thus the wavelengths of P and S-waves are roughly 15km and 9km, respectively, which is much larger than the size of the volcanic edifice. However, we cannot omit the effect of topography, because

topography can change even the relative location between sources and receivers. Ohminato and Chouet (1997) developed a FORTRAN code based on the finite difference method (FDM) for the computation of synthetic seismograms including free surface boundary conditions for arbitrary topography. Chouet et al. (2003) and Chouet et al. (2005) conducted waveform inversions of broadband seismic data obtained at Stromboli, Italy, and Popocatepetl, Mexico, respectively, taking into account the effect of topography using the above-mentioned FDM code.

Iwodake is a rhyolitic volcanic cone with a height of about 700 m, a radii of about 0.4 km at the top and about 1.5 km at its base. Fig.1(c) shows a bird's-eye view of the digitized topography of Satsuma-Iwojima. The source location of the VLP signals estimated from the particle velocity analyses is shallower than the three seismic stations at the base of Iwodake cone, and we therefore must incorporate the topography of Iwodake into the computations of Green's functions. A digitized elevation model (DEM) with a grid size of 17 m was used in the Green's function calculation.

Before conducting a grid search around the initial source location for the best-fit solution, Green's functions must be given at each grid point. Since the number of grid points that has to be searched is large, extensive computer resources are needed. To reduce the total computational cost, we made use of the reciprocity theorem (Aki and Richards, 1980). The reciprocal relation for source and receiver is shown by

$$G_{mn}(\mathbf{x}_1;\mathbf{x}_2) = G_{nm}(\mathbf{x}_2;\mathbf{x}_1) \tag{1}$$

where $G_{mn}(\mathbf{x}_1;\mathbf{x}_2)$ is the m-th component of displacement at $\mathbf{x}_1$ originating from the unit impulse applied at $\mathbf{x}_2$ in the n-direction. The reciprocity tells that the m-th component of displacement at $\mathbf{x}_1$ originating from the unit impulse applied at $\mathbf{x}_2$ in the n-direction is the same as the n-th component of displacement at $\mathbf{x}_2$ originating from the unit impulse applied at $\mathbf{x}_1$ in the m-direction. Instead of

computing Green's functions by putting a source at all the grid points one after another, we computed and stored at each grid point three displacement components from impulsive sources located at the positions of the eight stations. In our case, we needed to perform computer runs for eight receiver locations and three displacement components. Thus, we needed 8×3=24 computer runs total. An increase in the number of grid points N increases the required storage that is proportional to N, but the total number of computer runs is the same.

Suppose we have to compute the Green's functions at all the grid points to be searched without using the reciprocity theorem. Six moment tensor components and 3 single force components are needed for each source location, and we therefore need $9 \times N$ runs. The total number of computer runs is proportional to the number of grids N and thus easily exceeds the 24 runs that are required when the reciprocity theorem is used. We tested the reciprocity theorem by comparing the Green's functions computed with and without using the reciprocity theorem. In all the cases, the waveforms computed by these two different ways matched each other within a numerical error. There were some exceptional cases in which the waveforms computed by the two methods had discrepancies in the later portion of the waveforms. This happened when the later portion of the waveform was contaminated by an artificial reflection from numerical absorbing boundaries. The reason why the reciprocity theorem did not work perfectly for the later portion of some of the waveforms may be due to the fact that the homogeneous boundary condition that is required by the reciprocity theorem was not completely satisfied at the artificial absorbing boundary condition of Clayton and Engquist (1977) used in the FDM code.

We used the Green's functions computed by using the reciprocity theorem in the waveform inversions for the following reasons. First, the usage of reciprocity significantly reduces

the computational time. Second, the discrepancy between waveforms obtained in two different manners is small in the main portion of each of the Green's functions. The discrepancy in the latter portion of the Green's functions will not affect the results of the inversion significantly, due to its relatively small amplitude.

Fig.11 illustrates comparisons between the synthetic waveforms calculated for the model including realistic topography of Satsuma-Iwojima and those calculated for a laterally homogeneous 1D model. In Fig.11, *x*, *y*, and *z* correspond to the east-west, north-south and vertical component, respectively. In both cases, synthetic seismograms were calculated by the FDM code assuming an isotropic expansion source placed at a depth of 50 m below the ground surface. Synthetic seismograms with realistic topography were significantly affected by the topography in both amplitude and phase. The most marked feature seen in Fig.11 is that the amplitude of the horizontal *x*-component at ST1 computed with topography is several times larger than that of the same component computed without topography.

We adopted the inversion method developed by Ohminato et al. (1998) to analyze a seismic event recorded at Kilauea Volcano, Hawaii. We will briefly explain this method here. Assuming a time-dependent moment tensor, the *n*-th component of displacement can be written as (Chouet, 1996, eq. (8))

$$u_n(t) = F_p(t) * G_{np}(t) + M_{pq}(t) * G_{np,q}(t), \quad p,q = x,y,z, \tag{2}$$

where $F_p(t)$ is the time history of the force applied in the *p*-direction, $M_{pq}(t)$ is the time history of the *pq*-element of the moment tensor, and $G_{np}(t)$ is the Green tensor, which relates the *n*-component of displacement at the receiver position with the *p*-component of impulsive force at the source position. The notation *,q* implies spatial differentiation with respect to the *q*-coordinate, and *

denotes convolution. Summation over repeated indices is implied. This equation is discretized and the discretized weighting functions are unknowns to be determined. The discretized equations are written in matrix form and solved by using standard numerical packages.

4. Data analysis and results

The compressional and shear wave velocities used in the analyses were 3 and 1.8 km/s, respectively after Kamo (1976). We used the density of $\rho = 2.4 g/cm^3$ for degassed rhyolite in Satsuma-Iwojima after Kazahaya and Shinohara (1996). The heterogeneous velocity and density structure of the edifice of the Iwodake cone was not taken into consideration because: (i) we have no information on the velocity structure of Iwodake, and (ii) the wavelength of VLP pulses is long enough not to be affected by the heterogeneous velocity and density structure. Since the distances of all the observation stations from the source were shorter than or comparable to the wavelength under consideration, no anelastic attenuation was included in the calculation of Green's functions. Based on the results of the particle motion analysis, the initial source location was assumed to be 2 grid points (34 m) below the floor of the summit crater. We performed a grid search around the initial source location to find the best-fit source position. The optimum solution was chosen in terms of the variance reduction.

4.1. Inversion results

To evaluate the effect of topography on the inversion results, we performed two

inversions using two different sets of Green's functions: (1) using the velocity model with the topography of Satsuma-Iwojima, and (2) using the velocity model with a flat free surface. In the latter case, we didn't include elevation corrections because the elevations of the 4 base stations were below the source elevation and we could not apply the ordinary elevation correction equally to both the stations above the source and the stations below the source. For both cases, we used the same values of P and S wave velocities and density of the medium as stated above. After conducting a grid search around the initial source location, the best source location was found at a depth of 100 m beneath the floor of the summit crater. Figs.12 (a) and 12(b) show the source time functions obtained by the waveform inversions for both cases, with topography and without topography. The waveform matches for the two cases were very similar, and thus only the case with topography is shown in Fig.13. In the inversion, we used the same weight for each trace and thus the higher the amplitude of the trace was, the more the results were influenced. The signal observed at ST1 was prominent in its amplitude among the signals observed at eight stations, and thus it strongly governed the results of the inversion. The variance reductions for the two cases were almost the same, because the variance reduction came mainly from the waveform match of the ST1 data. The three velocity components at ST1 were almost perfectly explained in both cases.

Based solely on the variance reduction, it was difficult to say which solution was better. However, we could distinguish two solutions based on the amplitude ratio of the moment tensor components. Solutions with and without topography indicate that the three diagonal components (M_{xx}, M_{yy}, M_{zz}) of the moment tensor components have almost identical time histories and the off-diagonal components (M_{xy}, M_{yz}, M_{zx}) are small. The amplitude ratios of three eigenvalues obtained by the two inversions are shown in Table 1 with the orientation of the corresponding

eigenvectors. The amplitude ratio of the three eigenvalues are (5.9, 3.7, 2.9) × 10^{10} Nm ≈ (2±0.1, 1±0.2, 1±0.1) × 3.1 × 10^{10} Nm for the case with topography, and (15.7, 9.1, 3.4) × 10^{10} Nm ≈ (2±0.2, 1±0.3, 1±0.5) × 7.1 × 10^{10} Nm for the case without topography. Both solutions are characterized by the amplitude ratio of (2:1:1).

What kind of source geometry corresponds to the eigenvalue ratio of (2:1:1)? When the Poisson ratio $\nu = 1/4$, then the Lamé coefficients λ and μ are equal and the eigenvalue ratio corresponding to the crack opening is $(\lambda + 2\mu : \lambda : \lambda) = (3:1:1)$. If the Poisson ratio $\nu = 1/3$, then $\lambda = 2\mu$ and the amplitude ratio of the three eigenvalues corresponding to the crack opening is (2:1:1). The latter case of a high Poisson ratio may occur when the rock matrix in the vicinity of the crack is heated and has small rigidity (Ohminato et al. (1998), Chouet et al. (2003)). The solution which takes into account the topography can be interpreted as an opening of an inclined crack at the source region, as illustrated in Fig.14. The solution without topography can also be interpreted as an opening of a nearly vertical crack.

Both solutions, with and without topography, can be interpreted as a crack opening. However, the latter solution has a much larger discrepancy from the pure crack solution than the former. Recall that the *x*-component of the Green's function at ST1 is amplified owing to the topography. In the flat model case (or without topography), the observed eastward-oriented amplification may be attributed not to the effect of topography, but to the source. This explains why the largest eigenvalue in the case without topography is too large, and why the corresponding eigenvector is almost horizontal and oriented almost to the east. Thus, the solution corresponding to an inclined crack opening obtained by considering the effect of topography is much more plausible.

We omitted the contribution of the single force components to the observed waveforms

because its influence was minimal. The peak-to-peak amplitudes of the single force component and moment tensor component obtained by the inversion are of the order of 10^7N and 10^{11}Nm, respectively. In our case, numerical tests showed that the contribution of a single force component with a strength of approximately 10^7N was comparable to the contribution of a moment tensor component of 10^9Nm. Thus the contribution of the observed single force component is only 1% of the moment tensor components. The time histories of the single force components are shown in Figs.12 (a) and 12(b), but their contributions to the waveforms are not included in the following discussion.

5. Discussion

As was shown above, both slow and rapid physical processes contributed to the seismic signals observed at Satsuma-Iwojima. The periodic amplitude modulation of tremor and the long interval between VLP pulses are manifestations of the slow process, while the VLP pulses with rise-times of 3-4 s are considered to be manifestations of the rapid physical process. Moreover, the modulation pattern of the tremor amplitude differs from frequency to frequency, suggesting that the physical processes behind them are frequency-dependent. Furthermore, the results of the waveform inversion of the VLP pulses show that the force system applied at the source region corresponds to the opening of an inclined crack. The repetitive characteristics of tremor amplitude modulation and identical waveforms of VLP pulses strongly suggest that the above-mentioned source processes are non-destructive and repetitive. Any models of physical processes from which the observed seismic signals are emitted must satisfy these characteristics of waveforms.

How about simple discrete seismic events superimposed on a low-amplitude background tremor? What if the discrete events are broadband, and the volcano's medium has frequency-dependent intrinsic attenuation? If this is the case, it is still necessary to explain the regular interval of the "discrete seismic events." We also have to assume that such a "frequency-dependent attenuation" must also be "time-dependent," because the amplitude ratio of the IMF and HF-components are different in the Inc-Stage and Dec-Stage. It is more natural, we believe, to attribute the three different signals observed, the VLP, IMF-tremor and HF-tremor to three different mechanisms that are connected and interacting with each other.

Neuberg et al. (2000) analyzed tremor and low-frequency earthquakes observed at Soufriere Hills volcano in Montserrat. They modeled the shifting spectral lines of the seismic signals in terms of changes in the gas content of the magma as well as in terms of a time-dependent triggering mechanism of low-frequency resonances of a vertical conduit beneath a dome-shaped structure. Although their model seems to have a potential to explain the modulating tremor observed at Satsuma-Iwojima, it seems that the gas content of the magma in the resonating conduit needs to change periodically and abruptly.

As summarized in Fig.4 (b), the behaviors of the tremor amplitude modulation are classified into three types: VLP signals in the LF-range, amplitude modulations in the IMF-range, and amplitude modulations in the HF-range. The three types of modulation are all synchronized with one another, and the way they are synchronized obeys certain rules. We can confirm that the occurrence of VLP signals and the tremor amplitude modulation in the IMF and HF-ranges are synchronized only at a timing labeled as (1) in Fig.4 (b). On the other hand, we can confirm the synchronized occurrence of tremor amplitude modulations in the IMF and HF-ranges at two

timings labeled as (1) and (3) in Fig. 4. These observations suggest that the source system can be divided into two parts, one associated with VLP signals and the other associated with the IMF and HF-range signals. By taking this into consideration, we assume that the entire system is composed of an active part and a passive part. The active part corresponds to the behavior of VLP signals in the LF-range, while the passive part of the system corresponds to the other two behaviors in the IMF and HF-ranges. The active part is the part that generates VLP signals and drives the rest of the system. The passive part actually generates modulating tremors by responding to the driving part.

As a model of the active part, we consider a pressure source that exerts periodically varying pressure to the passive part. A temporal change in the pressure of the active part consists of two stages that occur alternately. One is a high-pressure stage, which corresponds to the Inc-Stage of the tremor amplitude modulation that lasts for about 10-15 min. The other stage is a low-pressure stage corresponding to the Dec-Stage of observed tremor amplitude modulation. The duration of this stage is about 30-35 min. As a model of the passive part, we consider a network of distributed gas-pockets connected by narrow gas-paths. One end of the network is attached to the pressure source via a valve whose opening and closure are controlled by pressure differences. The other ends of the network branch off in many directions. Each branch reaches the ground surface and is observed as an active fumarole.

5.1. Driving part of the source

We will start with an explanation of the model of the driving part. Our model is based on the sudden vaporization of water in a water pocket. In this model, a water-filled pocket beneath a

shallow aquifer works as a repetitive pressure source that drives the passive part of the whole system. The cyclic change in pressure is composed of two stages, a stage of sudden amplitude increase and a stage of gradual amplitude decrease. The pocket and the responding part are connected through a pressure-controlled valve. Water is supplied gradually to the pocket through bedrock with low permeability. The geometry of the pocket will be an inclined crack as suggested by the results of the waveform inversions of the VLP pulses.

Initially, the pocket is filled with water (Fig.15a). The water pocket and the narrow path are connected through a pressure-controlled valve. The pocket is heated by magma or high temperature volcanic gas. At this stage, the pressure in the pocket has not yet become high enough to open the valve, and thus there is no gas flow out of the pocket. When the water temperature exceeds the vaporization point, the water in the pocket is vaporized.

Note that if the water in the pocket is always in equilibrium, an increase in water temperature follows the phase diagram of water and no sudden pressure increase will occur. However, if the water in the pocket is superheated, the temperature of the water in the pocket can exceed the boiling temperature determined by the phase diagram without increasing the pressure. The more the water temperature increases, the more unstable the superheated state becomes. Finally, at a certain temperature, the superheated state will be broken and sudden vaporization and pressure increase will occur.

If the vaporization proceeds quickly enough, the increase in pressure will be observed as a VLP pulse. The valve opens and the vapor in the pocket starts to flow into the passive part composed of a dendritic gas path. We have no idea whether the valve itself excites the VLP signals when it opens. It will presumably work as a seismic source of the HF-tremor because the valve

itself chokes the gas flow. The sharp onset of the HF tremor corresponds to the beginning of this gas flow into the passive gas-path network (Fig.15b). The ground water in the permeable rock surrounding the pocket will also be pushed back some distance from the pressurized water pocket.

As the vapor starts escaping from the pocket, the pressure in the pocket starts declining. At the same time, the pressure in the gas chamber increases and the pressure difference at the two sides of the valve decreases. The ground water that was once pushed back from the pocket by the sudden pressure increase of the pocket permeates and gradually seeps back towards the pocket through the bedrock. It takes 15 minutes for the water to reach the surface of the pocket and start refilling the pocket again. Once the ground water starts entering the pocket, the pressure in the pocket declines rapidly due to the condensation of the vapor in the pocket back into water. The differential pressure at the valve then falls below a certain threshold. The valve then closes, and the vapor flow from the water pocket is terminated. This termination of the vapor flow corresponds to the end of the tremor modulation in the HF-range (Fig.15c). This 15 minute stage is observed as the Inc-Stage of the tremor amplitude modulation.

Water keeps being supplied gradually to the pocket through the surrounding rock, which has low permeability. At some point in time, the temperature in the pocket begins to increase rather than decrease, and the gradual water supply and temperature increase continue simultaneously. Initially, the temperature increase in the pocket will be slow because of the relatively low temperature of the refilling ground water. Once the pocket is filled with water and the water supply is terminated, the rate of temperature increase will accelerate. This is a stage preparing for the next cycle of expansion, and lasts for about 30 min (Fig.15d). The slowness of the process shown in our model is due to the low permeability of the surrounding rock.

5.2 Passive part of the source

We will now explain the passive part of the system that generates tremor in response to the active pressure source explained above. In our model, it is assumed that the gas flow in a narrow constricted path can generate seismic signals. It is also assumed that the tremor amplitudes are the function of the gas flow rate through the path, namely, as the gas flow rate increases, the amplitude of the tremor also increases. The tremor-generating gas flow through a narrow constriction is modeled by Morrissey and Chouet (1997), who conducted extensive numerical simulations of an excitation of seismic signals by fluid flow through a narrow constriction. There have been several other reports arguing that volcanic tremor originates from a gas flow through a constricted portion of the gas path inside volcanoes (e.g., Steinberg and Steinberg, 1975; Chouet et al., 1994).

Presumably, an actual gas path that connects the pressure source and the ground surface is composed of a sequence of swollen portions and constricted portions of the path, as schematically illustrated in Fig.16 (a). Each swollen portion of the gas path works as a small gas chamber or a gas pocket along the path. Each constricted portion of the gas path works as a resistance to the fluid flow through the path. We considered a simplified model composed of a gas chamber and two constrictions connected in series instead of dealing with the above-mentioned complicated dendritic geometry of the gas path. Then the whole model, including both the active and the passive parts, is regarded as a serial connection of a pressure source, a pressure controlled valve, a narrow constriction, a gas chamber, and another narrow constriction, as shown in Fig.16

(b).

The differential equations that describe the above-mentioned model take the following form.

$$\begin{cases} q_1 = \dfrac{1}{R_1}\left(p_s - p_c\right) \\ q_2 = \dfrac{1}{R_2}\left(p_c - p_a\right) \\ \dfrac{dp_c}{dt} = \dfrac{1}{C}\left(q_1 - q_2\right) \end{cases} \tag{3}$$

where q_1 is the gas flow rate from the pressure source to the small gas chamber through the pressure controlled valve, q_2 is the flow rate from the gas chamber to the atmosphere, p_s represents the pressure of the pressure source, p_c is the pressure in the chamber, and p_a is the atmospheric pressure. R_1, R_2 are positive constants representing the resistance to the gas flow q_1 and q_2, respectively. C is a positive constant representing the chamber capacity to the gas. The first two equations of (3) indicate that the flow rates are proportional to the pressure differences. The third equation of (3) shows that the pressure change in the chamber is proportional to the total gas flow rate into or out of the chamber. We assume that the lengths of the amplitude increasing stage (Inc-Stage) and the decreasing stage (Dec-Stage) are Δt_1 and Δt_2, respectively. Then the start time of Inc-Stage is represented as $t = n\Delta t_0$, where n is an integer and $\Delta t_0 = \Delta t_1 + \Delta t_2$. The Inc-Stage lasts from $t = n\Delta t_0$ to $t = n\Delta t_0 + \Delta t_1$. The Dec-Stage starts at $t = n\Delta t_0 + \Delta t_1$ and ends at $t = (n+1)\,\Delta t_0$.

We will show that the solutions to (3) well mimic the behavior of the seismic tremors schematically shown in Fig.4 (b) under the following assumptions. (i) The source pressure p_s is higher than the atmospheric pressure p_a. (ii) $R_2 \gg R_1$ and thus $q_1 \gg q_2$, so that the gas is stored in the chamber during the Inc-Stage. If this condition is not satisfied, then the gas travels through the

gas-path to the ground surface without being trapped by the chamber, and thus no Inc-stage. (iii) In the Dec-Stage, the valve is closed due to the small pressure difference between the source and the chamber, and thus, q_1 is zero. (iv) The change in the source pressure p_s is small compared to the change of the chamber pressure p_c during the Inc-Stage, and thus p_s can be regarded as a constant during the Inc-Stage. (v) The value of p_s is always the same for all n.

The simplest model for the gas flows through the valve or through the gas-path network will be Poiseuille flow of viscous fluid through a cylindrical pipe. In this case, the resistance is proportional to the fluid viscosity and is inversely proportional to the cross-sectional area of the pipe. Our assumption that $R_2 \gg R_1$ corresponds to the condition that the cross-section of the valve is much larger than the smallest cross-section of the gas-paths.

First, we will obtain the chamber pressure p_c. The general form of p_c as a solution to (3) will be

$$p_c = A_n + B_n e^{-t/\tau_n}, \quad (n = 1,2,3,\cdots), \tag{4}$$

where A_n and B_n are some constants decided with given initial conditions. τ_n are time constants. The value of τ_n differs in the Inc-Stage and Dec-Stage. While n is small, A_n and B_n varies with n, but these coefficients A_n and B_n approach some constants after some cycles have elapsed. At the limit of $n \to \infty$, p_c in the Inc-Stage of different time windows, $n\Delta t_0 \le t \le n\Delta t_0 + \Delta t_1$ (n = 1,2,3…), will have the same shape time-shifted by Δt_0. The same can be said for the solutions to (3) in the Dec-Stage of different time windows. The limiting values of A_n and B_n are easily obtained by solving simultaneous linear equations that are obtained from the condition that the chamber pressure p_c is continuous at the boundary between the Inc-Stage and Dec-Stage. Once the chamber pressure p_c is obtained, then the gas flow rates q_1 and q_2 are given by the first two equations of (3).

The solutions to (3) at the limit of $n \to \infty$ are as follows.

$$q_1 = A_1\left(1 + B_1 e^{-t_1/\tau_1}\right) \qquad \text{in Inc-Stage} \tag{5}$$

$$q_1 = 0 \qquad \text{in Dec-Stage} \tag{6}$$

$$q_2 = A_2\left(1 - B_2 e^{-t_1/\tau_1}\right) \qquad \text{in Inc-Stage} \tag{7}$$

$$q_2 = A_2 e^{-t_2/\tau_2} \qquad \text{in Dec-Stage} \tag{8}$$

where t_1 and t_2 are the time measured from the beginning of the Inc-Stage and Dec-Stage, respectively. $\tau_1 = CR_1R_2/\left(R_1 + R_2\right)$ and $\tau_2 = CR_2$ are time constants of the change in chamber pressure during the Inc-Stage and Dec-Stage, respectively, and A_1, A_2, A_3, B_1 and B_2 are positive constants and are given as

$$A_1 = \frac{R_2\left(p_s - p_a\right)}{R_1\left(R_1 + R_2\right)}, \qquad B_1 = \frac{R_1}{R_2} \cdot \frac{1 - e^{-\Delta t_2/\tau_2}}{1 - e^{-\gamma}}$$

$$A_2 = \frac{R_1\left(p_s - p_a\right)}{R_2\left(R_1 + R_2\right)}, \qquad B_2 = \frac{1 - e^{-\Delta t_2/\tau_2}}{1 - e^{-\gamma}}$$

$$A_3 = \frac{R_1\left(p_s - p_a\right)}{R_2\left(R_1 + R_2\right)} \cdot \frac{1 - e^{-\Delta t_1/\tau_1}}{1 - e^{-\gamma}}, \qquad \gamma = \frac{\Delta t_1}{\tau_1} + \frac{\Delta t_2}{\tau_2}.$$

The solution (5) represents an exponentially decreasing curve. See the portion that is labeled (2) in the middle panel of Fig.4 (b) (HF tremor). Note that $B_1 \ll 1$ since $R_2 \gg R_1$. It means that the amount of decrease of q_1 is small compared to its initial value. This feature is manifested as

a characteristic envelope of the tremor amplitude modulation in the HF-range in the Inc-Stage. q_1=0 in the Inc-Stage also matches the behavior of tremor amplitude modulation in the HF-range. See the portion that is labeled (4) in the middle panel of Fig.4 (b) (HF tremor). On the other hand, the solution (7) represents an increasing curve with a gradually decreasing rate of increase, as seen in the tremor amplitude modulation of the IMF-range in the Inc-Stage, while solution (8) represents an exponentially decreasing curve, as is seen in the IMF-range modulation in the Dec-Stage. See the top panel of Fig.4 (b) (IMF tremor). Thus, the characteristics of q_1 and q_2 represented by eqs. (5)-(8) well explain the behavior of the HF tremor and IMF tremor, respectively, in both the Inc-Stage and Dec-Stage.

5.3. Different frequency peaks

The dominant frequency peaks seen in the IMF-range differ from station to station, while some peaks are the same for all of the stations (Fig.8). The different frequency peak locations from station to station may be explained by the path effect, but the same peaks for all stations cannot be explained solely by the pass effect. How does our model explain these observations?

The frequency peaks common to all the stations can be interpreted as a source effect, while the different peaks cannot be explained as a source effect. They will be explained as follows. In the above-mentioned model, narrow constricted portions of the gas paths are distributed between the pressure source and the ground surface. Each constricted portion works as a tremor source. Since the geometrical properties of each constricted portion differ from each other, they will have different dominant spectral peaks. Suppose that a constricted portion characterized by a certain

dominant frequency is located close to ST1, and another constriction with a different dominant frequency is located in the vicinity of ST2. Then the observed dominant frequencies at ST1 and ST2 will be different, although amplitude modulations at both stations are synchronized. In Fig. 16, this situation is schematically indicated.

5.4. Water pocket model and geochemical observations

The water pocket model discussed above and the geochemical observations conducted at Satsuma-Iwojima so far are not consistent with each other. One contradiction is the temperature of the volcanic gas. The temperature of the steam emitted from the water pocket should be near the boiling temperature under the pressure at the source depth. As the lithostatic pressure at the estimated source depth of 100 m is roughly 3 Mp, the vaporization temperature of the water at the depth is 234°C. However, the temperatures of the fumarolic gas measured in the summit area of Iwodake are nearly 900°C (Shinihara et al., 2002). Another contradicting point is the geochemical composition of the water. Although our water pocket requires cold water and the candidate for it is meteoric water, the chemical composition of the fumarolic gas is of magmatic origin (Hedingquest et al., 1994).

One possible remedy for these contradictions is that the amount of meteoric water involved in the water pocket model is only a fraction of the total amount of the volcanic gas emitted from the summit area of Iwodake, and thus the meteoric water may not have been well detected by the geochemical measurements conducted so far. In other words, the paths of water flow of meteoric origin and of magmatic origin are different. The observed seismic moment of VLP pulses

is roughly 3×10^{10}Nm. The volume change corresponding to this seismic moment is 4.3 m^3. At the boiling temperature of 234°C, the mass of the steam of 4.3 m^3 is about 80 kg. As the averaged number of VLP events per day is around 30, the amount of water participating in the activity is only 2.4 t/day, which is negligibly small compared to the 1.6×10^4 t/day of H_2O emitted from the summit (Kazahaya et al., 2002). The fact that the water volume estimated from the seismic signals is only a fraction of the amount of water estimated by the geochemical measurement supports the abovementioned possible remedy.

5.5 A source model other than the water pocket model

In order to explain the huge amount of volcanic gas emitted from Satsuma-Iwojima, it is hypothesized that a gigantic magma reservoir exists beneath the island and that magma convection in the volcanic conduit is an efficient magma transportation mechanism from the deep reservoir to the shallower part of the volcano (Kazahaya and Shinohara, 1996; Kazahaya et al., 2002). We here consider a source process associated with magma convection in the volcanic conduit. First, we will briefly explain the magma convection model proposed by Kazahaya et al. (1994). In the magma convection model, magma is supplied through a conduit from a deep reservoir to the shallower depth by its own buoyancy. When magma reaches a certain depth at which the magma pressure is lower than the degassing pressure, H_2O, SO_2 and other volatiles exsolve from the magma. Since the degassed magma is denser than the gas-rich fresh magma, it starts sinking down through the upwelling fresh magma. Consequently, degassed magma is returned to the deep magma chamber and fresh magma rises to replenish the shallower part of the conduit. By this simple mechanism,

gas-rich magma is efficiently transported to the shallow part of the volcanoes and a huge volcanic gas emission is maintained.

The sudden volume expansion observed as VLP signals may be related to the release of surface tension resulting from the coalescence of bubbles that are accumulated in the gas-rich magma at the top of the conduit. The pressure in each bubble is higher than the ambient pressure. The differential pressure between inside and outside the bubbles is proportional to the surface tension and is reciprocally proportional to the radius of the bubbles (Leighton, 1994). When bubbles coalesce into a single bubble, the volume of the resultant single bubble must be larger than the volume sum of the coalesced smaller bubbles in order to compensate for the weaker surface tension provided by the larger radius. The bubble would keep swallowing adjacent bubbles and eventually burst, allowing internal volcanic gas to be emitted. If the magma transportation rate is constant, then this expansion-emission process would occur at a regular interval. The water pocket model discussed above can be substituted by the model of bubble expansion and gas emission associated with magma convection in the conduit. Bubble dynamics are poorly understood and a quantitative discussion of this model will be left open.

6. Conclusions

We conducted broadband seismic observations at Satsuma-Iwojima using a seismic network in which 5 short period and 3 broadband sensors were deployed. A regular periodicity in the amplitude modulation of the volcanic tremor and the occurrence of VLP pulses was observed at intervals ranging from 46 to 50 min.

Observed waveforms have characteristics that strongly depend on their frequency range. For all the frequency ranges, the repetition period is about 46 to 50 minutes. In a high frequency-range above 40 Hz, a sharp beginning of the amplitude increase followed by a slow amplitude decay was observed. The high amplitude stage of this frequency band lasts for about 15 minutes. In the intermediate frequency range from 1 Hz to 40 Hz, amplitude modulation is composed of two stages. One is a gradual amplitude increasing stage with an upward convex envelope lasting for about 15 minutes. The other is an amplitude-decreasing stage with a concave shape of the envelope lasting for about 30 minutes. In the low frequency range below 0.2 Hz, very long period (VLP) seismic signals are observed. These signals are pulse shaped, and their pulse width is roughly 3-4s. All the observed pulses have almost identical waveforms. Although the patterns of amplitude modulation are different from frequency range to frequency range, they are all perfectly synchronized.

Waveform inversions applied to the VLP signals revealed that the mechanism of inclined crack opening occurring at about a depth of 100 m from the bottom of the summit crater best explains the observed VLP waveforms.

Both periodical tremor modulation and VLP signals are well explained by the model of a heated water pocket that has a pressure-controlled valve, although there are some difficulties explaining geochemical observations using this model. In this model, water is supplied to the pocket from the surrounding shallow aquifer through low permeable rock. In terms of this model, the observed periodical occurrences of VLP signals are explained by the sudden vaporization of superheated water in a shallow water pocket. The inferred tremor source is a network of gas pockets connected by narrow constricted paths. When an impulsive pressure increase due to

vaporization in the water pocket is asserted on the network of the gas paths, the gas flow rate through the network mimics the observed amplitude modulation of the volcanic tremor in the intermediate frequency range.

References

Aki, K., Richards, P.G., 1980. Quantitative Seismology, W.H. Freeman and Co., San Francisco, CA, 932pp.

Almendros, J., Chouet, B., Dawson, P., 2001. Spatial extent of a hydrothermal system at Kilauea Volcano, Hawaii, determined from array analyses of shallow long-period seismicity. I. Method, J. Geophys. Res. 106, 13565-13580.

Almendros, J., Chouet, B., 2003. Performance of the Radial semblance method for the location of very long period volcanic signals, Bull. Seism. Soc. Am. 93, 1890-1903.

Aster, R., Mah, S., Kyle, P., McIntosh, W., Dunbar, N., Johnson, J., Ruiz, M., McNamara, S., 2003. Very long period oscillations of Mount Erebus Volcano, J. Geophys. Res. 108(B11), 2522,doi:10.1029/2002JB002101.

Benoit, J., McNutt, S., 1997. New constraints on source processes of volcanic tremor at Arenal Volcano, Costa Rica, using broadband seismic data, Geophys. Res. Lett. 24, 449-452.

Chouet, B., Page, R., Stephens, C., Lahr, J., Power, J., 1994. Precursory swarms of long-period events at Redoubt Volcano (1989-1990), Alaska: their origin and use as a forecasting tool, J. Volcanol. Geotherm. Res. 62, 95-135.

Chouet, B.A., 1996. New methods and future trends in seismological volcano monitoring, in *Monitoring and Mitigation of Volcano Hazards*, Scarpa, R., Tilling, R., ed., Springer-Verlag, New York, pp. 23-97.

Chouet, B., Saccorotti, G., Dawson, P., Martini, M., Scarpa, R., De Luca, G., Milana, G., Cattaneo, M., 1999. Broadband measurements of the sources of explosions at Stromboli Volcano, Italy,

Geophys. Res. Lett. 26, 1937-1940.

Chouet, B, Dawson, P., Ohminato, T., Martini, M., Saccorotti, G., Giudicepietro, F., De Luca, G., Milana, G., Scarpa, R., 2003. Source mechanisms of explosions at Stromboli volcano, Italy, determined from moment-tensor inversions of very-long-period data, J. Geophys. Res. 108(B1),2019,doi:10.1029/2002JB001919.

Chouet, B., Dawson, P., Arciniega-Ceballos, A., 2005. Source mechanism of vulcanian degassing at Popocatepetl Volcano, Mexico, determined from waveform inversions of very long period signals, J. Geophys. Res. 110,B07301,doi:10.1029/2004JB003524.

Clayton, R., Engquist, B., 1977. Absorbing boundary conditions for acoustic and elastic wave equations, Bull. Seism. Soc. Am. 67, 1529-1540.

Cruz-Atienza, V.M., Pacheco, J.F., Singh, S.K., Shapiro, N.M., Valdes, C., Iglesias, A., 2001. Size of Popocatepetl volcano explosions (1997-2001) from waveform inversion, Geophys. Res. Lett. 28, 4027-4030.

Hedenquist, J., Aoki, M., Shinohara, H., 1994. Flux of volatiles and ore-forming metals from the magmatic-hydrothermal system at Satsuma Iwojima volcano, Japan, Geology 22, 585-588.

Kamo, K.,1976, Seismic observation, in Feasibility study on volcano electric power plant. Research report of commissioned survey on Sunshine project, 38-59 (in Japanese).

Kamo, K., Furuzawa, T., Akamatsu, J., 1977. Some natures of volcanic micro-tremors at the Sakurajima volcano, Bull. Volcanol. Soc. Japan 22, 41-48, (in Japanese with English abstract).

Kawakatsu, H., Kaneshima, S., Matsubayashi, H., Ohminato, T., Sudo, Y., Tsutsui, T., Uhira, K., Yamasato, H., Oikawa, J., Takeo, M., Iidaka, T., 2000. Aso 94: Aso seismic observation with broadband instruments, J. Volcanol. Geotherm. Res. 101, 129-154.

Kazahaya, K., Shinohara, H., Saito, G., 1994. Excessive degassing of Izu-Oshima volcano: magma convection in a conduit, Bull. Volcanol. 56, 207-216.

Kazahaya, K., Shinohara, H., 1996. Excess degassing of active volcanoes: process and mechanisms, Mem. Geol. Soc. Japan 46, 91-104 (in Japanese with English abstract).

Kazahaya, K., Shinohara, H., Saito, G., 2002. Degassing process of Satsuma-Iwojima volcano, Japan: Supply of volatile components from a deep magma chamber, Earth Planets Space 54, 327-335.

Kedar, S., 1996. The origin of harmonic tremor at Old Faithful Geyser, PhD Thesis, Caltech, Pasadena.

Kedar, S., Sturtevant, B., Kanamori, H., 1996. The origine of harmonic tremor at Old Faithful Geyser, Nature, 379, 708-711.

Kieffer, S., 1984. Seismicity at Old Faithful Geyser: an isolated source of geothermal noise and possible analogue of volcanic seismicity, J. Volcanol. Geotherm. Res. 22, 59-95.

Legrand, D., Kaneshima, S., Kawakatsu, H., 2000. Moment tensor analysis of near field broadband waveforms observed at Aso volcano, Japan, J. Volcanol. Geotherm. Res. 101, 155-169.

Leighton, T.G., 1994. The Acoustic Bubbles, 613 pp., Academic Press, New York.

Machida, H., Arai, F., 1992. Atlas of Tephra in and around Japan, University of Tokyo Press, p.48 (in Japanese).

McNutt, S.R.,1996. Seismic monitoring and eruption forecasting of volcanoes: A review of the state-of-the-art and case histories, in *Monitoring and Mitigation of Volcano Hazards*, Scarpa, R., Tilling, R., ed., Springer-Verlag, New York, pp.99-146.

Mori, J., Patia, H., McKee, C., Itikarai, C., Lowenstein, P., De Saint Ours, P., Talai, B., 1989.

Seismicity associated with eruptive activity at Langila Volcano, papua New Guinea. J. Volcanol. Geotherm. Res. 38, 243-255.

Morrissey, M., Chouet, B., 1997. A numerical investigation of choked flow dynamics and its application to the triggering mechanism of long-period events at Redoubt volcano, Alaska, J. Geophys. Res. 102, 7965-7983.

Neidel, N., Tarner, M.T., 1971. Semblance and other coherency measure for multichannel data. Geophysics 36, 483-497.

Neuberg, J., Luckett, R., Ripepe, M., Braun, T., 1994. Highlights of a seismic broadband array on Stromboli volcano, Geophys. Res. Lett. 21, 749-752.

Neuberg, J., Luckett, R., 1996. Seismo-volcanic sources on Stromboli volcano, Annali di Geofisica 39, 377-391.

Neuberg, J., Luckett, R., Baptie, B., Olsen, K., 2000. Models of tremor and low-frequency earthquake swarms on Montserrat, J. Volcanol. Geotherm. Res. 101, 83-104.

Nakano, M., Kumagai, H., Chouet, B., 2003. Source mechanism of long-period events at Kusatsu Shirane Volcano, Japan, inferred from waveform inversion of the effective excitation functions, J. Volcanol. Geotherm. Res. 122, 149-164.

Nishimura,T., Nakamichi, H., Tanaka, S., Sato, M., Kobayashi, T., Ueki, S., Hamaguchi, H., Ohtake, M., Sato, H., 2000. Source process of very long period seismic events associated with the 1998 activity of Iwate Volcano, northeastern Japan, J. Geophys. Res. 105, 19135-19147.

Ohminato, T., Chouet, B., 1997. A free-surface boundary condition for including 3D topography in the finite difference method, Bull. Seism. Soc. Am. 87, 494-515.

Ohminato, T., Ereditato, D., 1997. Broadband seismic observation at Satsuma-Iwojima volcano,

Japan, Geophys. Res. Lett. 24, 2845-2848.

Ohminato, T., Chouet, B., Dawson, P., Kedar, S., 1998. Waveform inversion of very-long period impulsive signals associated with magmatic injection beneath Kilauea Volcano, Hawaii, J. Geophys. Res. 103, 23839-23862.

Powell, T., Neuberg, J., 2003. Time dependent features in tremor spectra, J. Volcanol. Geotherm. Res. 128, 177-185.

Rowe, C.A., Aster, R.C., Kyle, P.R., Schlue, J.W., Dibble, R.R., 1998. Broadband recording of Strombolian explosions and associated very-long-period seismic signals on Mount Erebus volcano, Ross Island, Antarctica, Geophys. Res. Lett. 25, 2297-2300.

Rowe, C.A, Aster, R.C., Kyle, P.R., Dibble, R.R., Schlue, J.W., 2000. Seismic and acoustic observations at Mount Erebus volcano, Ross Island, Antarctica, 1994-1998, J. Volcanol. Geotherm. Res. 101, 105-128.

Schlindwein, V., Wassermann, J., Scherbaum, F., 1995. Spectral analysis of harmonic tremor signals at Mt. Semeru volcano, Indonesia. Geophys. Res. Lett. 22, 1685-1688.

Shinohara, H., Kazahaya, K., Saito, G., Matsushima, N., Kawanabe, Y., 2002. Degassing activity from Iwodake rhyolitic cone, Satsuma-Iwojima volcano, Japan: Formation of a new degassing vent, 1990-1999, Earth Planets Space 54, 175-185.

Steinberg, G., Steinberg, A., 1975. On possible causes of volcanic tremor, J. Geophys. Res. 80, 1600-1604.

Uhira, K., Takeo, M., 1994. The source of explosive eruptions of Sakurajima volcano, Japan, J. Geophys. Res. 99, 17775-17789.

Yamamoto, M., Kawakatsu, H., Yomogida, K., Koyama, J., 2002. Long-period (12 sec) volcanic

tremor observed at Usu 2000 eruption: Seismological detection of a deep magma pluming system, Geophys. Res. Lett. 29, 1329, doi: 10.1029/2001GL013996.

Yoshida, M., Ozawa, T., 1981. Amounts of some chemical components discharged from Satsuma Iwojima volcano in relation to their feeding sources, Bull. Volcanol. Soc. Japan 26, 25-34 (in Japanese with English abstract).

Figure captions

Fig.1. (a) Location of Satsuma-Iwojima, southern Kyushu, Japan. The Kikai caldera is also shown by a broken line. (b) Station locations. The three closed circles are the broadband stations and the five open circles are the short-period stations. (c) Bird's-eye view of Satsuma-Iwojima.

Fig.2. (Top) Five-hour record of vertical components of velocity at ST1 and ST3. The sensors at ST1 and ST3 are CMG-40T and L4, respectively. A trace low-pass filtered (LO) at 0.2 Hz is also shown in between the two unfiltered records. (Bottom) Expansion of the 1 min portion of the top panel. The sensor responses have not been removed.

Fig.3. Spectrogram of 8-hour record of vertical component at ST1. Frequency range is from 0 to 1 Hz. The three data gaps are due to the storage limitation. The window length and the time shift are both 120s. The corresponding seismic trace is also shown at the bottom. A broad energy peak between 0.3 and 0.6 Hz and a peak just below 0.2 Hz correspond to microseisms. The equal interval signals below 0.15 Hz marked by arrows are VLP pulses. In the time domain, these VLP pulses are buried in the microseisms and are barely seen in the bottom trace.

Fig.4. (a) Vertical component at ST1 at different frequency ranges. From the top to the bottom, an unfiltered trace, an envelope of the top trace, a high-pass filtered trace at 40 Hz, and a low-pass filtered trace at 0.2 Hz. Trace length is 280 min. Arrows at the bottom indicate VLP pulses that are clearly seen in the low-pass filtered trace. (b) Schematic diagrams representing an amplitude modulation of the tremor on the left. From the top to the bottom, an envelope, a high-pass filtered trace, and a low-pass filtered trace.

Fig.5. Spectrogram of a 180 min record of 200 Hz sampling data at ST1. The window length and

time shift are both 30 s. The tremor amplitude modulation in the frequency range higher than 40 Hz is characterized by sharp beginnings and sharp ends. In contrast, the beginnings and ends of the tremor amplitude modulation below 40 Hz are unclear.

Fig.6. Spectrogram for 3-hour record of volcanic tremor from 15:21 to 18:21 for stations ST1 and ST2. The window length and time shift are both 30 s. Amplitude modulation occurs over a wide frequency range. There are several stable spectral bands. Their positions differ from station to station.

Fig.7. Spectrogram for 3-hour record of volcanic tremor from 15:21 to 18:21 for stations ST3 and ST4. The window length and time shift are both 30s. Amplitude modulation occurs over a wide frequency range. There are several stable spectral bands. Their positions differ from station to station.

Fig.8. (a) A stacked spectra of volcanic tremor. Sixty-eight windows are extracted from a 3 hour record of volcanic tremor and are stacked. The window length is 100 sec and each window does not include tectonic events. (b) A stacked spectra of tectonic earthquakes. Seventeen events during the same 3-hour record are extracted and their spectra are stacked.

Fig.9. Improvement of signal-to-noise ratio by stacking. Vertical component of velocity at (a) ST1 and (b) ST8. At each column, the first five traces are traces before or during the stacking and the bottom trace is the result. Thirteen traces are stacked to generate the traces at the bottom. After stacking, a downward initial motion at ST8 is clearly seen.

Fig.10. Schematic diagram of the Iwodake cone with the velocity vector at three component stations, ST1, ST6 and ST7. Both the top-view (top) and sectional view (bottom) are shown.

Fig.11. Comparison of synthetic seismograms computed under two different conditions: with

topography (thick line) and without topography (thin line). An isotropic expansion source beneath the summit crater at the depth of 40 m is assumed. *z*, *x*, and *y* components refer to the vertical, east-west, and north-south component, respectively.

Fig.12. (a) Source-time functions of six moment tensor components and three single force components obtained with inclusion of actual topography. (b) Same as (a) but without topography.

Fig.13. Waveform match obtained with inclusion of actual topography of Satsuma-Iwojima for thirteen traces used in the inversion. ST1, ST6, and ST7 are the three component stations. The other stations have a vertical component only. The station code and its component are indicated at the upper left of each seismogram. The number at the upper right corner of each panel indicates the peak-to-peak amplitude of each seismogram. Unit of the amplitude is 10^{-7} m/s.

Fig.14. Source mechanism obtained for the case with topography.

Fig.15. A model of the VLP pulses and HF tremor. (a) The crack-shaped pocket beneath the shallow aquifer is filled with water. Its temperature increases gradually due to heat from the magma or hot volcanic gas. The water in the pocket reaches the superheated state. (b) When the temperature exceeds the boiling point by a certain amount, the superheated state is broken, and the water in the pocket is suddenly vaporized causing a pressure jump in the pocket. This sudden pressure increase may correspond to an occurrence of the VLP signal. The valve opens and the gas flow out of the pocket generates HF tremors. (c) After 15 min, the pressure in the pocket is reduced. The valve closes and terminates the vapor flow. (d) Water starts refilling the pocket, which takes about 30 min due to the low permeable bedrock.

Fig.16. (a) Schematic diagram of an irregularly shaped gas path with many swollen and constricted portions. (b) Simplified model of the tremor generating system composed of a pressure source, constrictions and a chamber.

Fig.17. A network of gas pockets and constrictions, which generates a volcanic tremor with frequency peaks which differ from place to place.

Table caption

Table 1. Source mechanisms of VLP events.

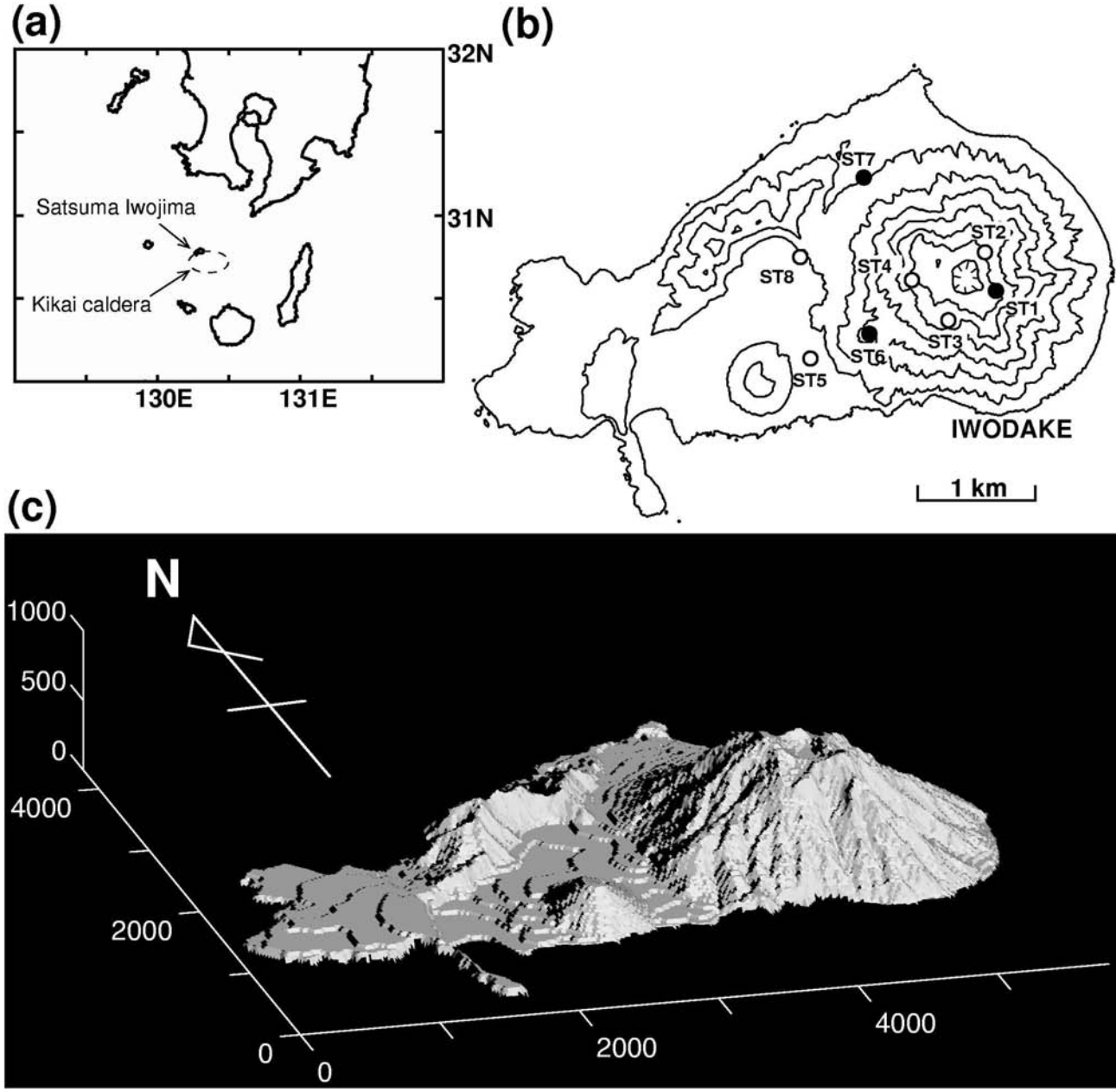
(a)
32N
31N
Satsuma Iwojima
Kikai caldera
130E
131E
(b)
ST7
ST2
ST4
ST8
ST1
ST3
ST6
ST5
IWODAKE
1 km
(c)
N
1000
500
0
4000
2000
0
0
2000
4000

Fig.1

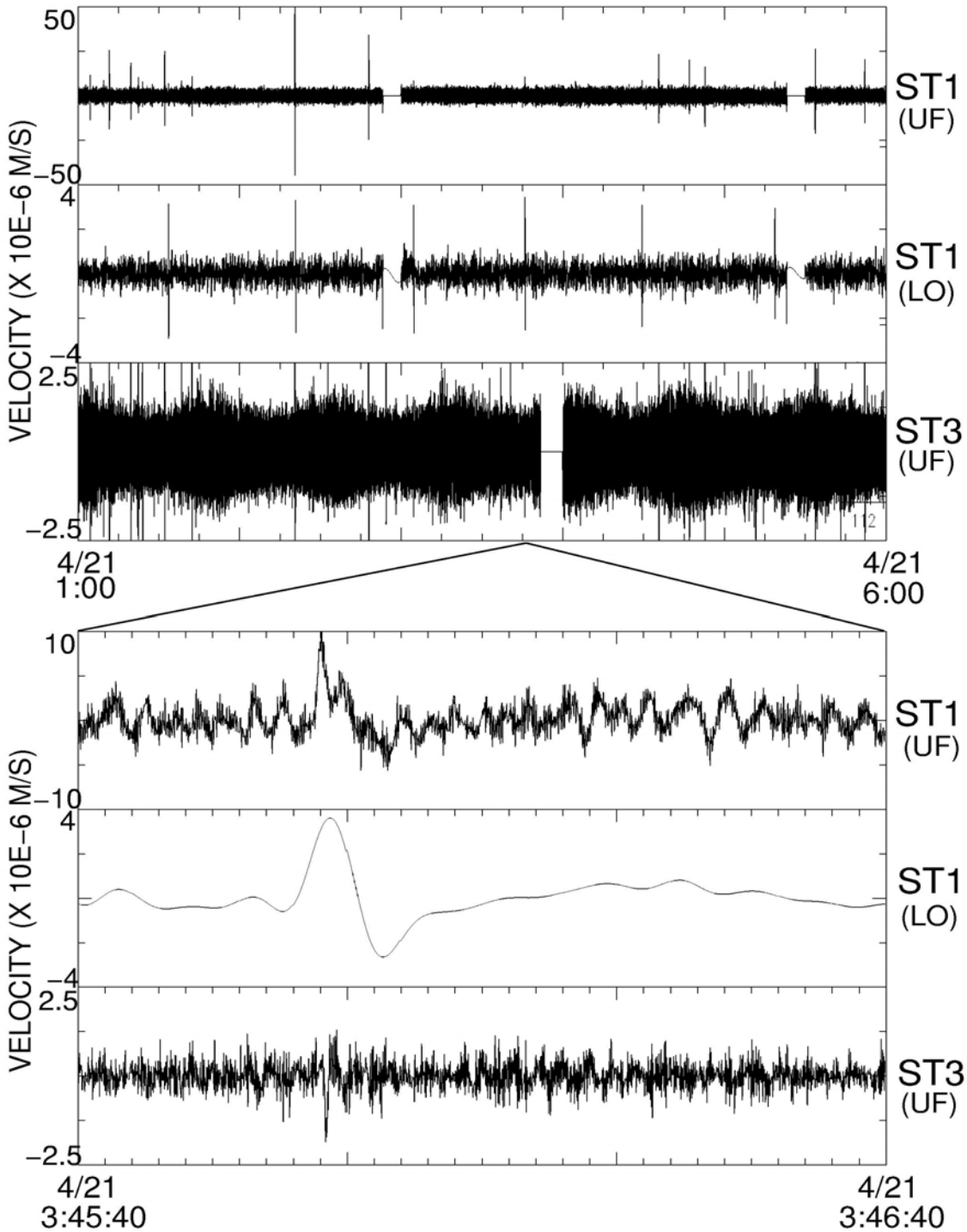
50
−50
4
−4
2.5
−2.5
VELOCITY (X 10E−6 M/S)
ST1
(UF)
ST1
(LO)
ST3
(UF)
4/21
1:00
4/21
6:00
10
−10
4
−4
2.5
−2.5
VELOCITY (X 10E−6 M/S)
ST1
(UF)
ST1
(LO)
ST3
(UF)
4/21
3:45:40
4/21
3:46:40

Fig.2

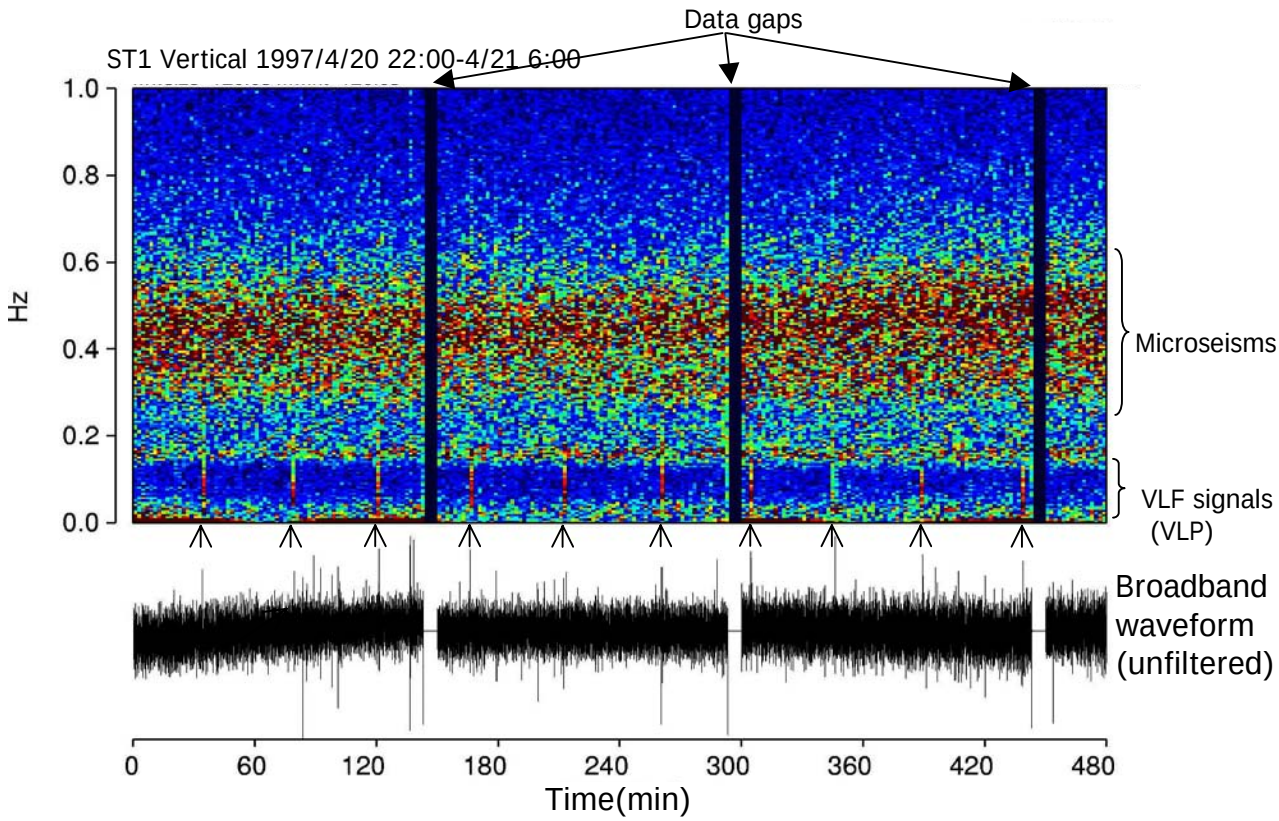
Data gaps
ST1 Vertical 1997/4/20 22:00-4/21 6:00
1.0
0.8
0.6
0.4
0.2
0.0
Hz
Microseisms
VLF signals
(VLP)
Broadband
waveform
(unfiltered)
0
60
120
180
240
300
360
420
480
Time(min)

Fig.3

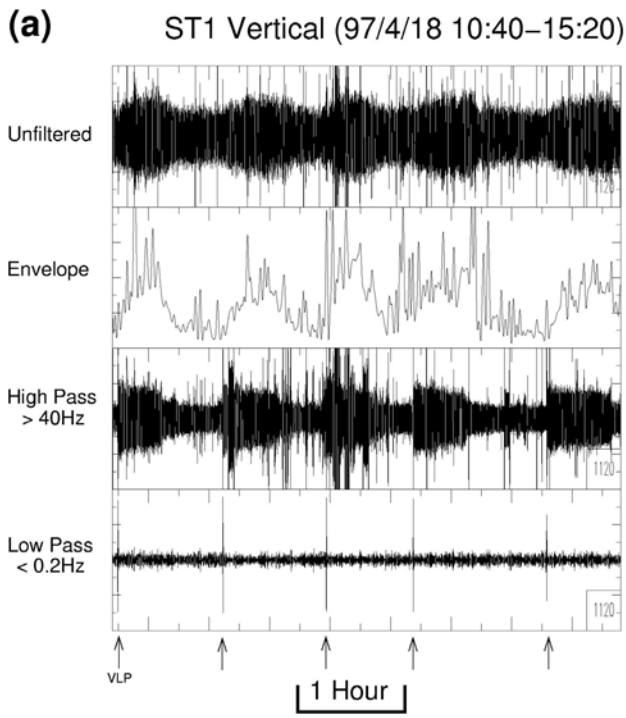
(a)
ST1 Vertical (97/4/18 10:40–15:20)
Unfiltered
Envelope
High Pass
> 40Hz
Low Pass
< 0.2Hz
VLP
1 Hour

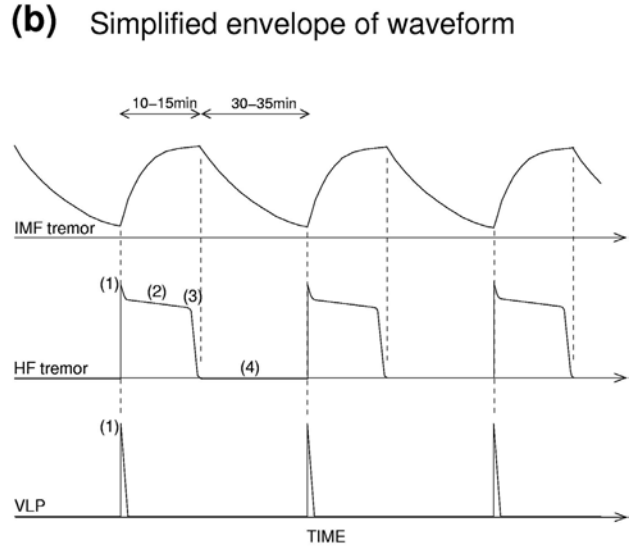
(b)
Simplified envelope of waveform
10–15min
30–35min
IMF tremor
(1)
(2)
(3)
(4)
HF tremor
(1)
VLP
TIME

Fig.4

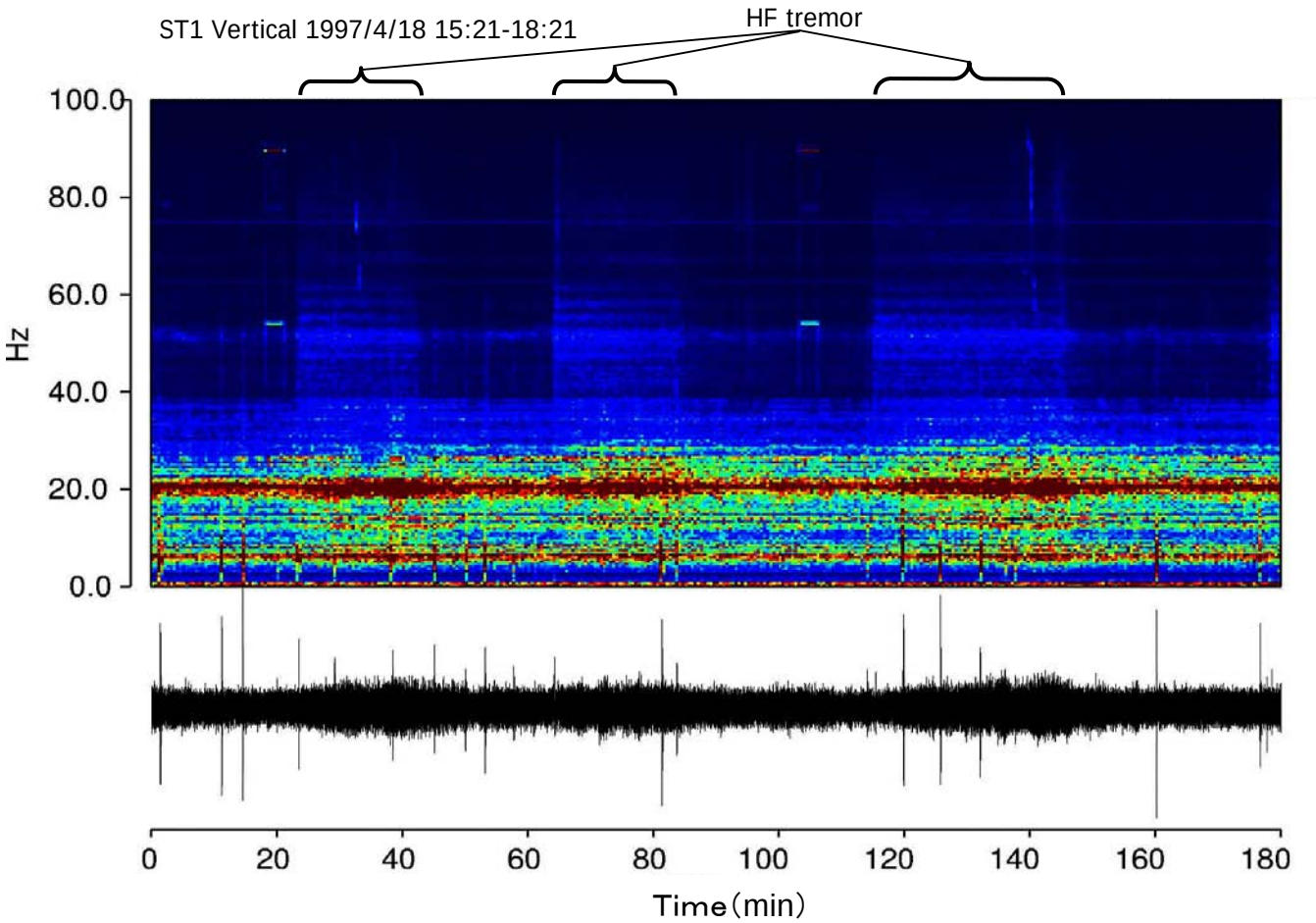
ST1 Vertical 1997/4/18 15:21-18:21
HF tremor
100.0
80.0
60.0
40.0
20.0
0.0
Hz
0
20
40
60
80
100
120
140
160
180
Time(min)

Fig.5

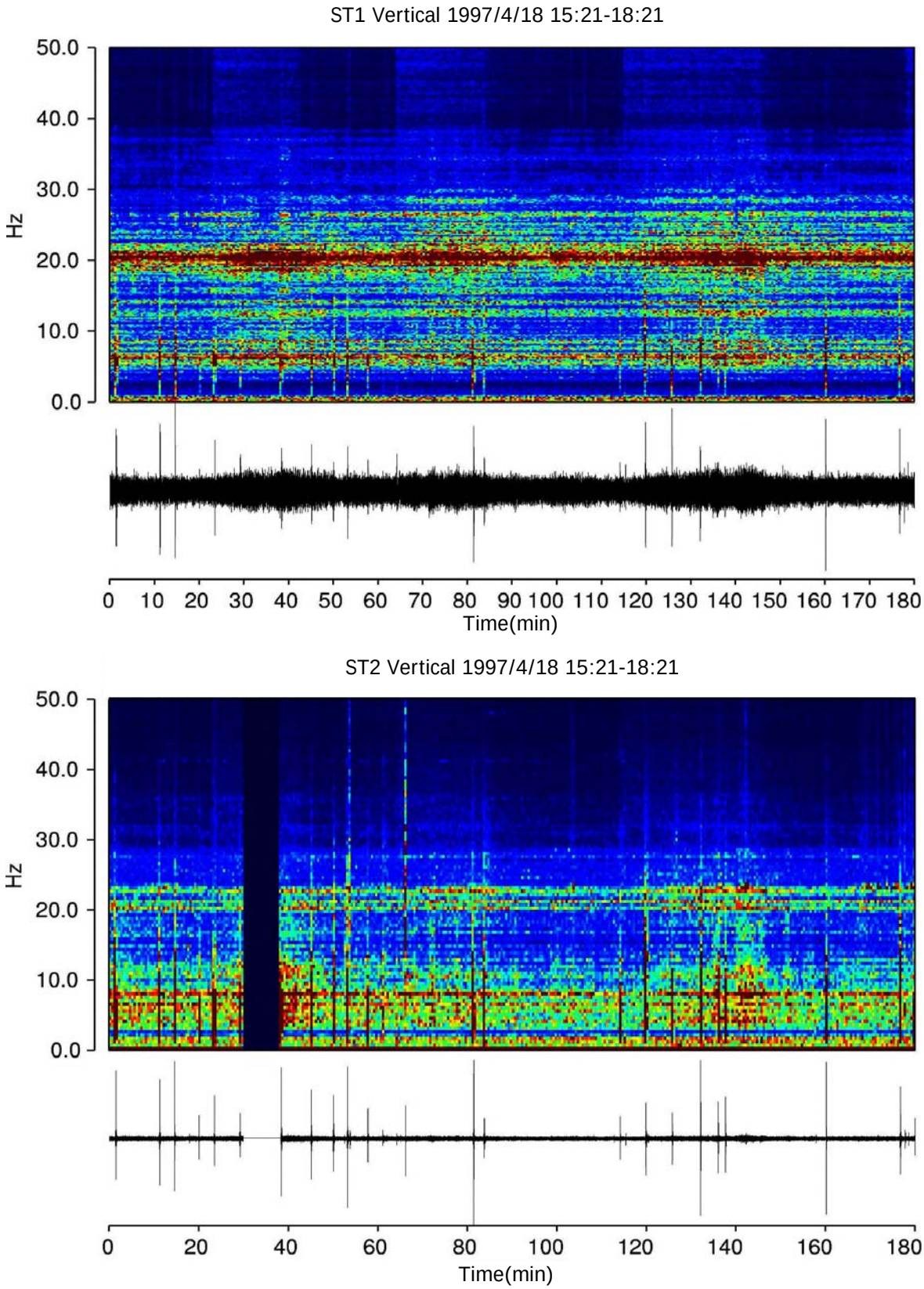
ST1 Vertical 1997/4/18 15:21-18:21
50.0
40.0
30.0
20.0
10.0
0.0
Hz
0 10 20 30 40 50 60 70 80 90 100 110 120 130 140 150 160 170 180
Time(min)
ST2 Vertical 1997/4/18 15:21-18:21
50.0
40.0
30.0
20.0
10.0
0.0
Hz
0 20 40 60 80 100 120 140 160 180
Time(min)

Fig.6

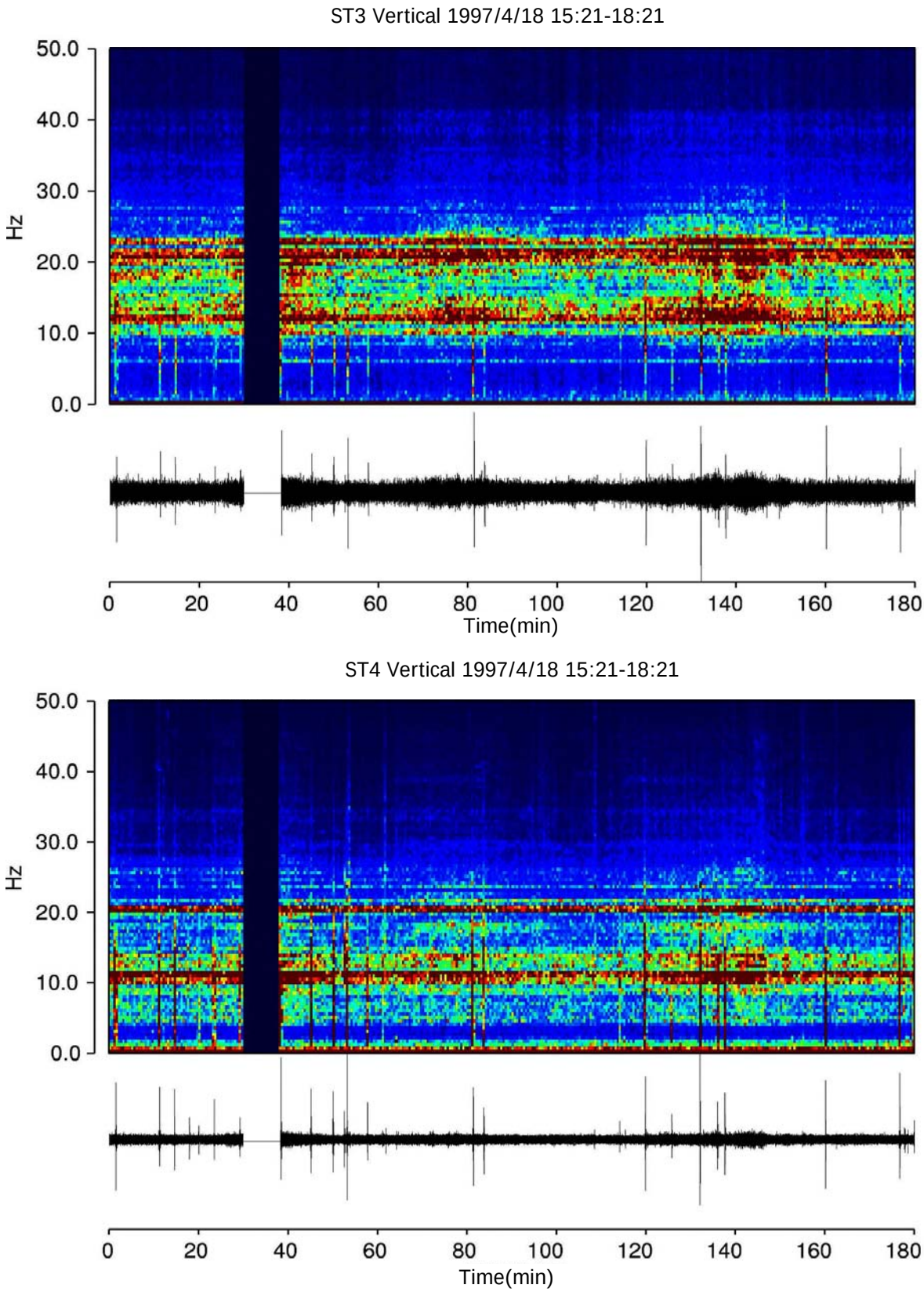
ST3 Vertical 1997/4/18 15:21-18:21
50.0
40.0
30.0
20.0
10.0
0.0
Hz
0
20
40
60
80
100
120
140
160
180
Time(min)
ST4 Vertical 1997/4/18 15:21-18:21
50.0
40.0
30.0
20.0
10.0
0.0
Hz
0
20
40
60
80
100
120
140
160
180
Time(min)

Fig.7

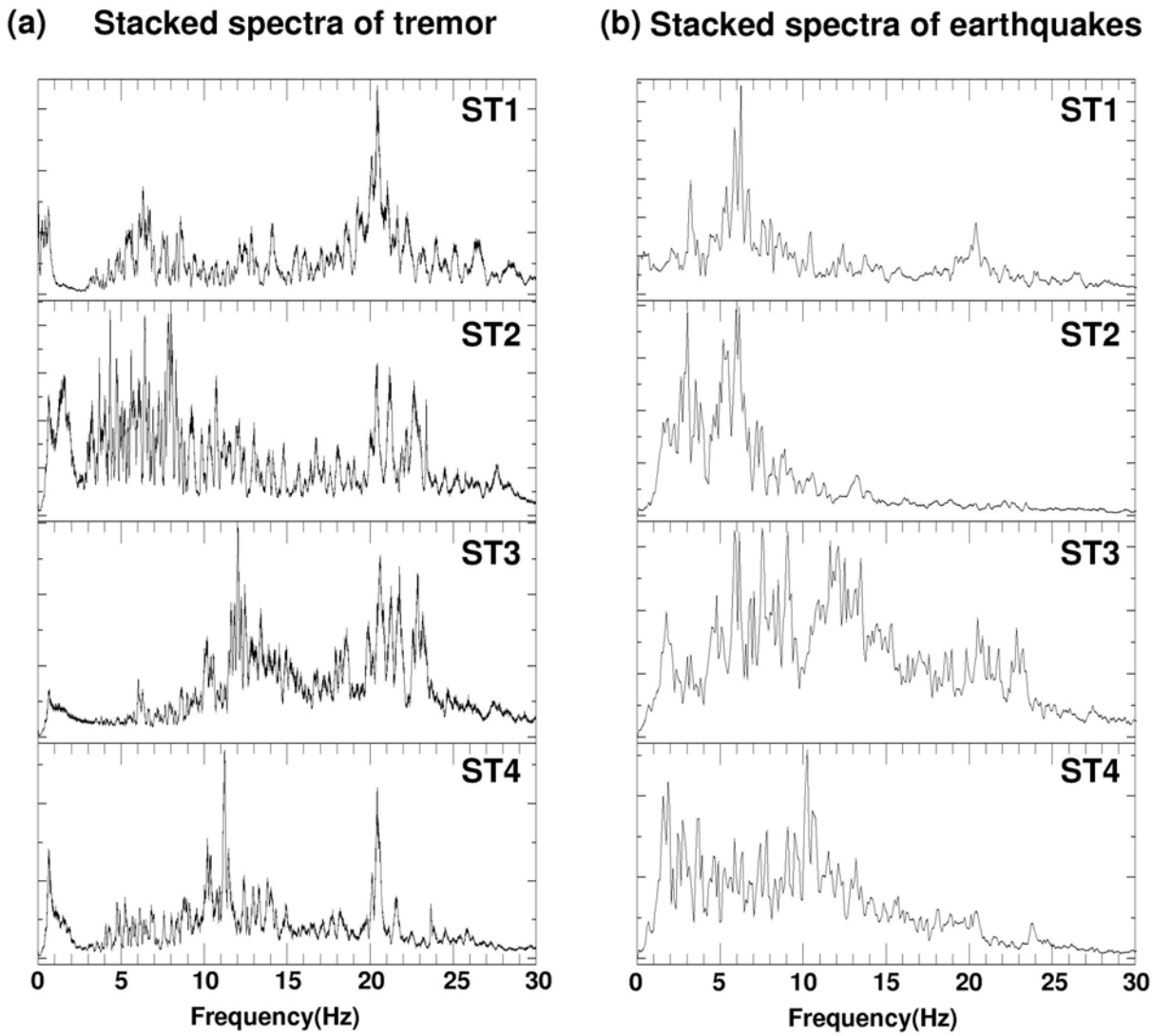
(a) Stacked spectra of tremor
(b) Stacked spectra of earthquakes
ST1
ST2
ST3
ST4
0
5
10
15
20
25
30
Frequency(Hz)

Fig.8

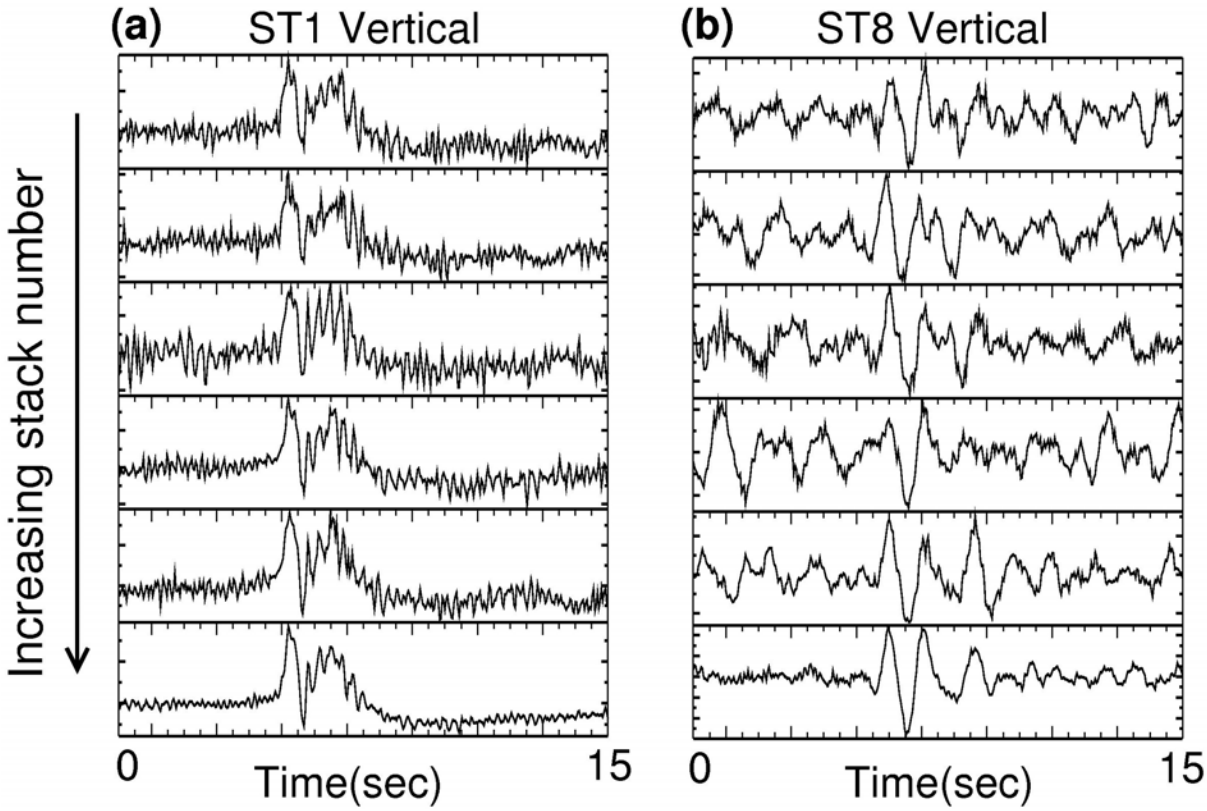
(a)
ST1 Vertical
(b)
ST8 Vertical
Increasing stack number
0
Time(sec)
15
0
Time(sec)
15

Fig.9

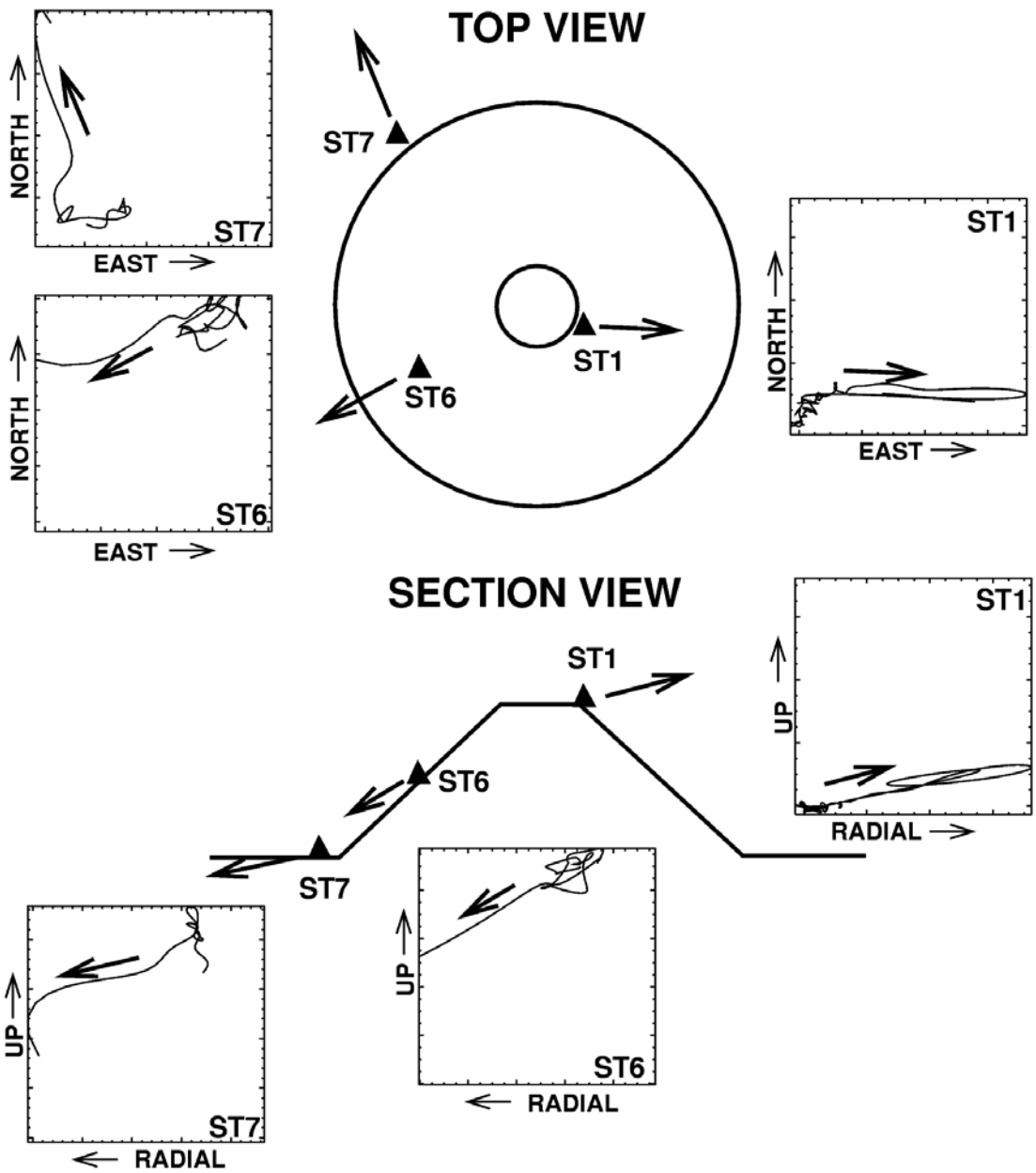
TOP VIEW
ST7
ST6
ST1
NORTH
EAST
ST7
NORTH
EAST
ST6
NORTH
EAST
ST1
SECTION VIEW
ST1
ST6
ST7
UP
RADIAL
ST1
UP
RADIAL
ST6
UP
RADIAL
ST7

Fig.10

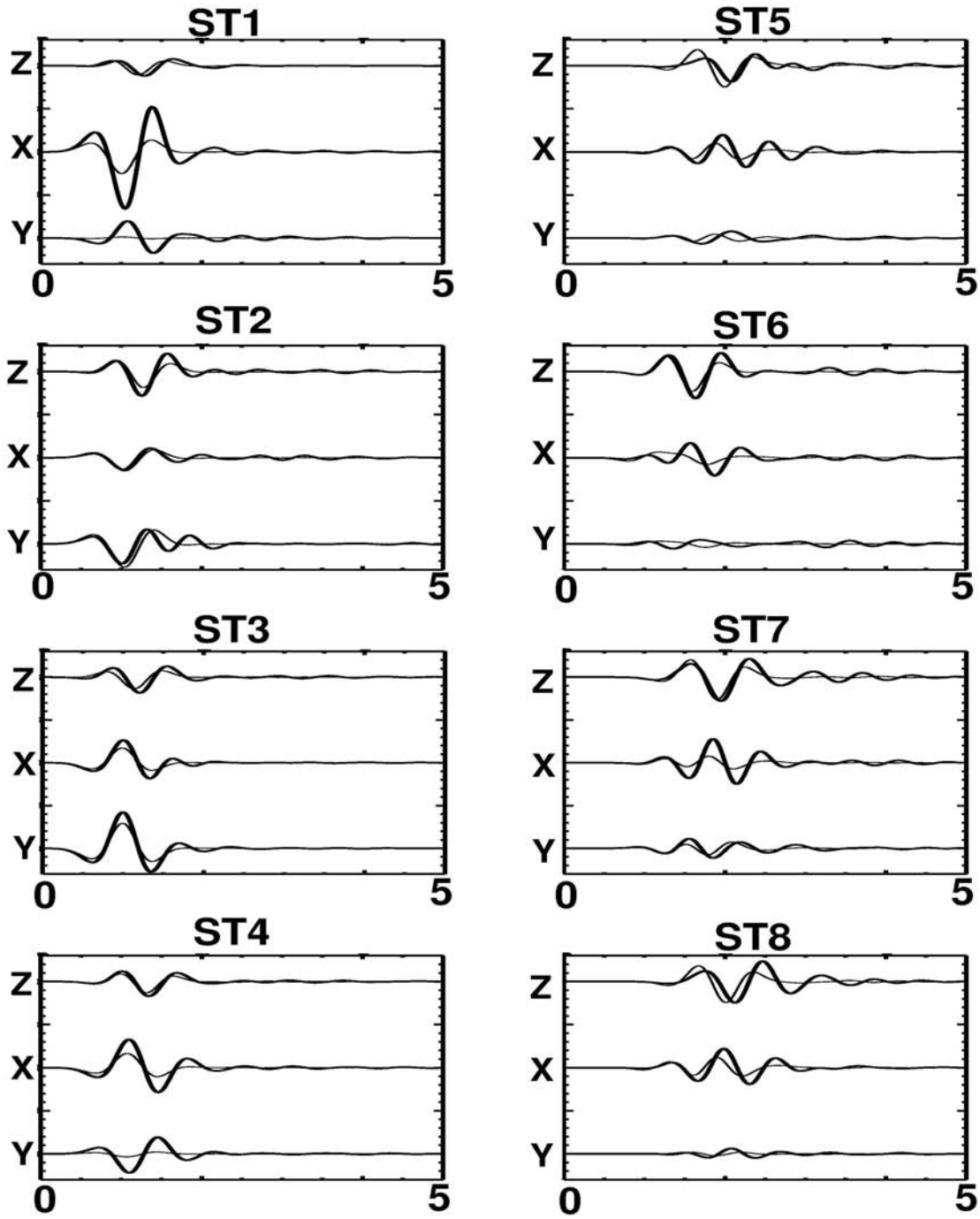
ST1
Z
X
Y
0
5
ST5
ST2
ST6
ST3
ST7
ST4
ST8
With topography
No topography

Fig.11

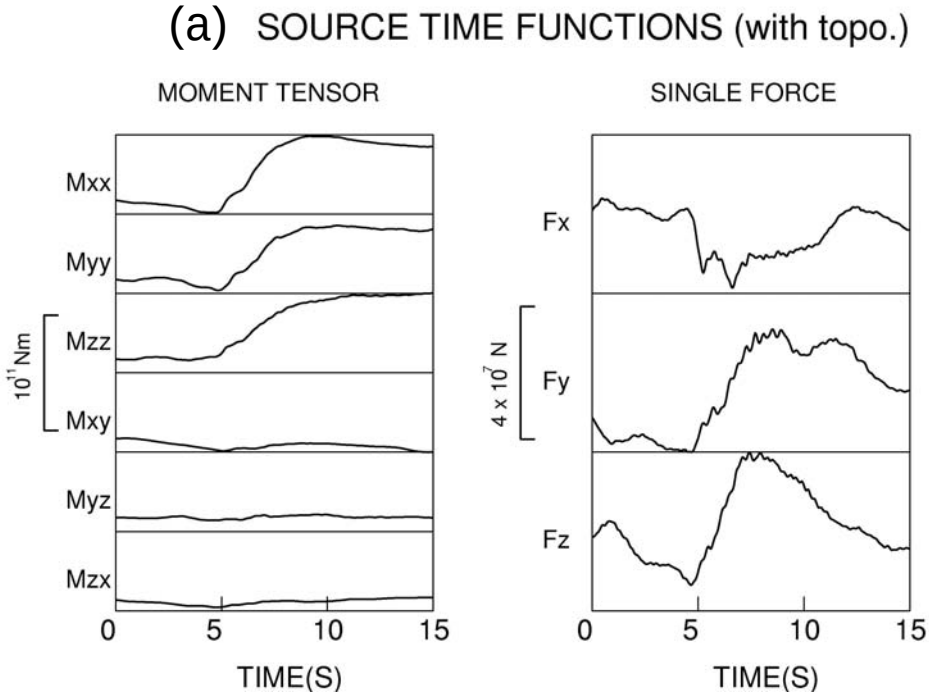
(a) SOURCE TIME FUNCTIONS (with topo.)
MOMENT TENSOR
SINGLE FORCE
Mxx
Myy
Mzz
Mxy
Myz
Mzx
10^11 Nm
Fx
Fy
Fz
4 x 10^7 N
0
5
10
15
TIME(S)

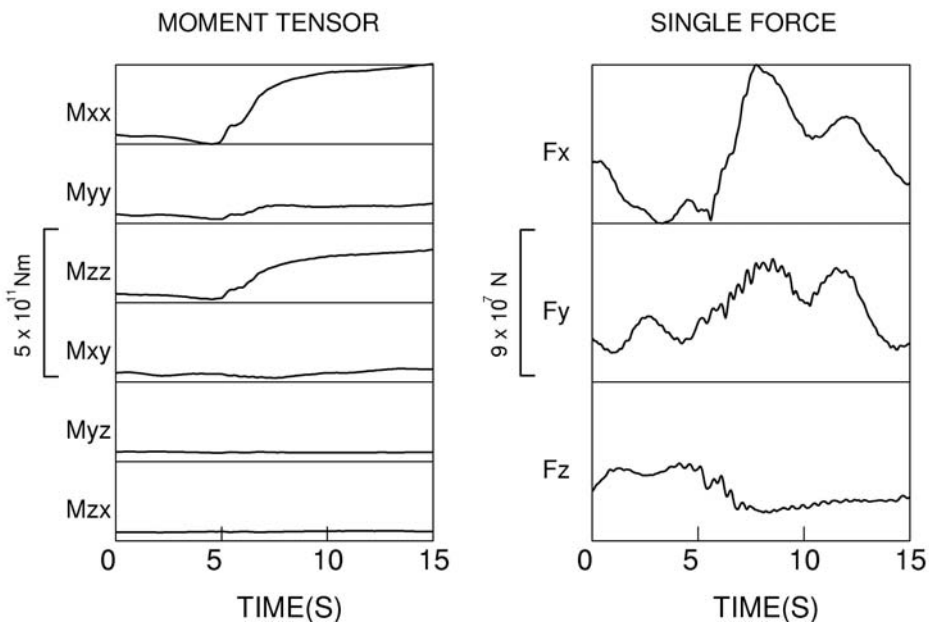
(b) SOURCE TIME FUNCTIONS (without topo.)
MOMENT TENSOR
SINGLE FORCE
Mxx
Myy
Mzz
Mxy
Myz
Mzx
5 x 10^11 Nm
Fx
Fy
Fz
9 x 10^7 N
0
5
10
15
TIME(S)

Fig.12

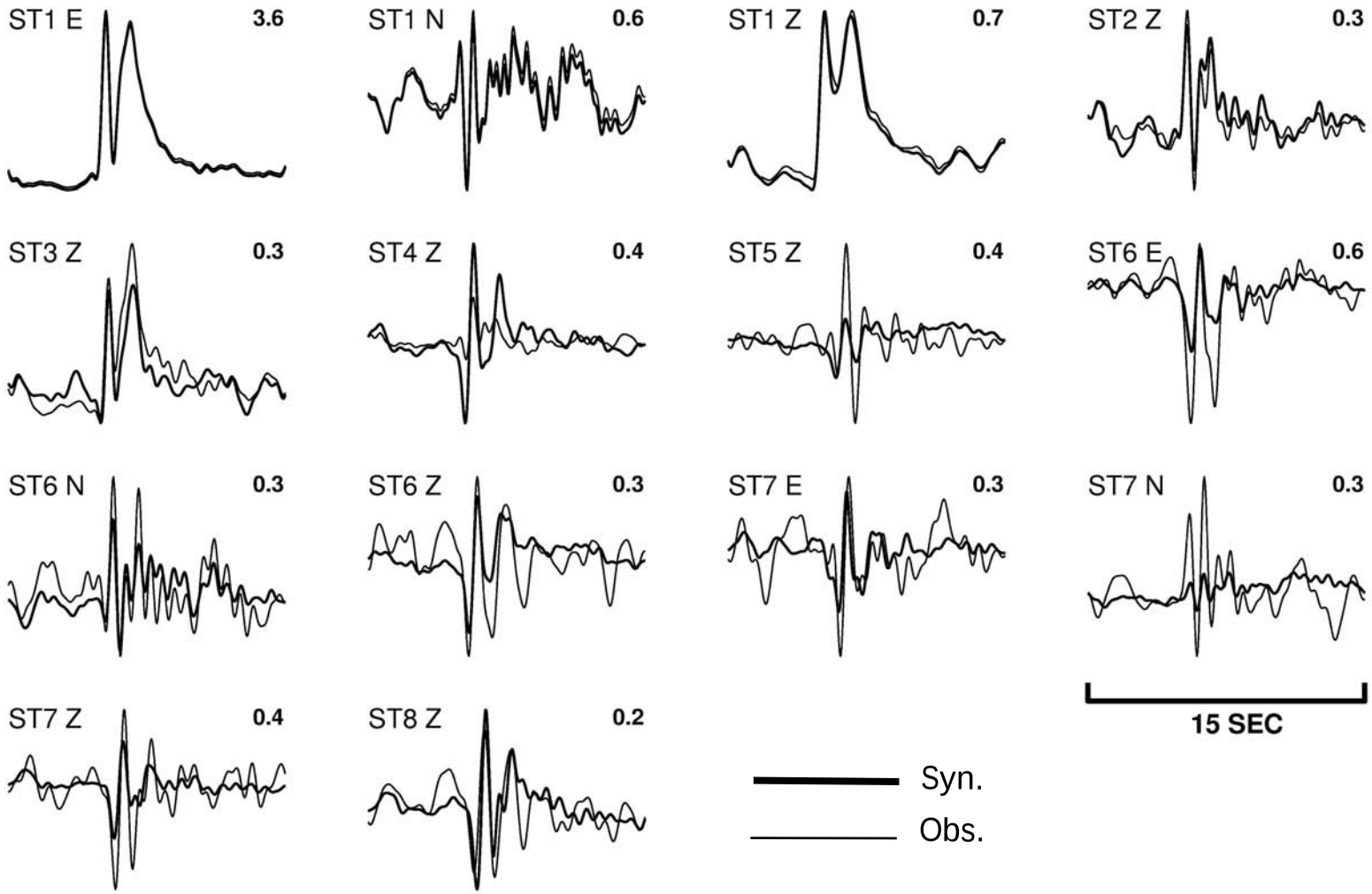
ST1 E
3.6
ST1 N
0.6
ST1 Z
0.7
ST2 Z
0.3
ST3 Z
0.3
ST4 Z
0.4
ST5 Z
0.4
ST6 E
0.6
ST6 N
0.3
ST6 Z
0.3
ST7 E
0.3
ST7 N
0.3
ST7 Z
0.4
ST8 Z
0.2
15 SEC
Syn.
Obs.

Fig.13

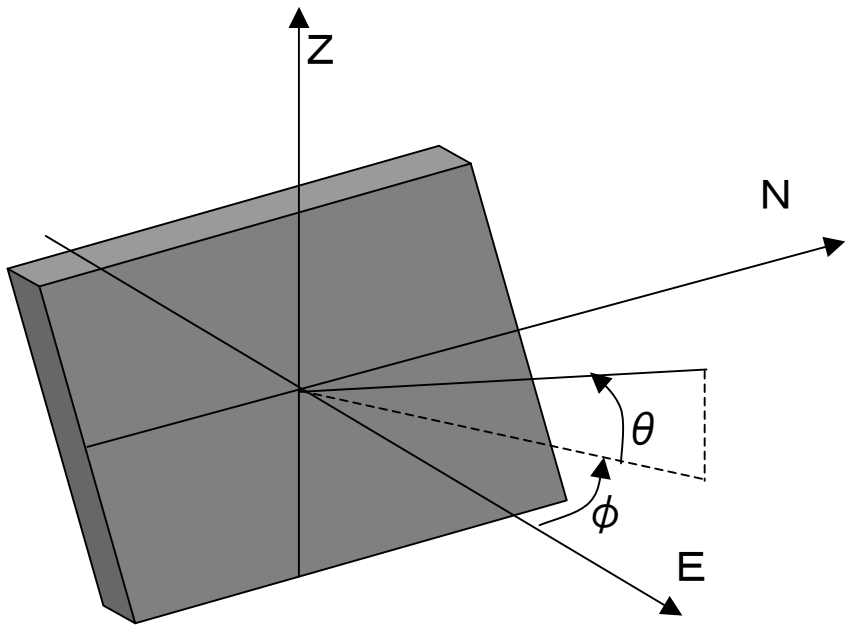

Inclined crack
（2±0.1:1±0.2:1±0.1）×3.1･10^{10}Nm

Fig.14

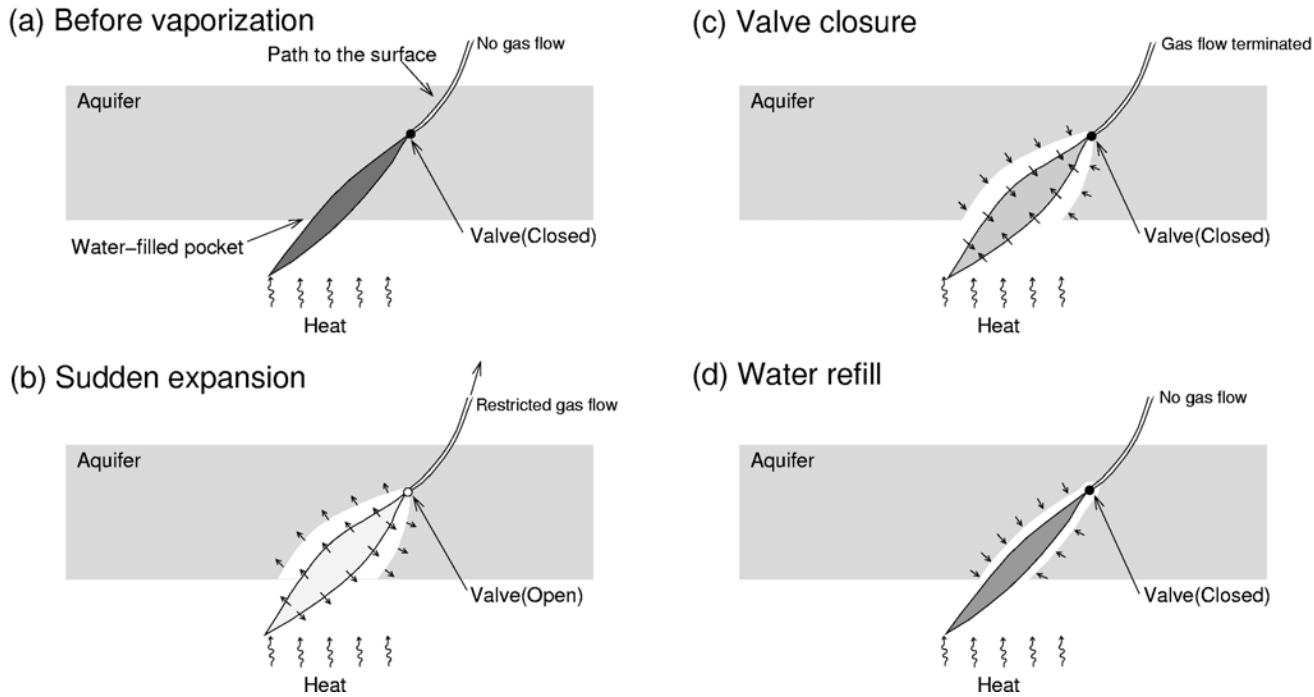
(a) Before vaporization
Path to the surface
No gas flow
Aquifer
Water–filled pocket
Valve(Closed)
Heat
(b) Sudden expansion
Restricted gas flow
Aquifer
Valve(Open)
Heat
(c) Valve closure
Gas flow terminated
Aquifer
Valve(Closed)
Heat
(d) Water refill
No gas flow
Aquifer
Valve(Closed)
Heat

Fig.15

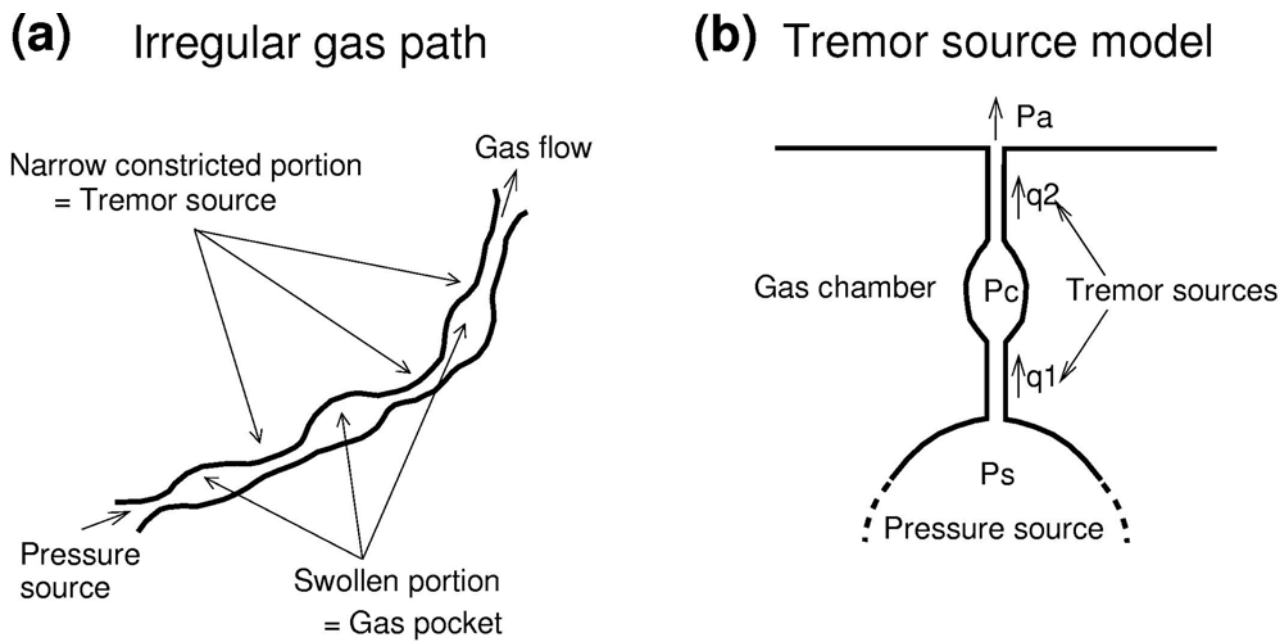
(a) Irregular gas path
Narrow constricted portion
= Tremor source
Gas flow
Pressure
source
Swollen portion
= Gas pocket
(b) Tremor source model
Pa
q2
Gas chamber
Pc
Tremor sources
q1
Ps
Pressure source

Fig.16

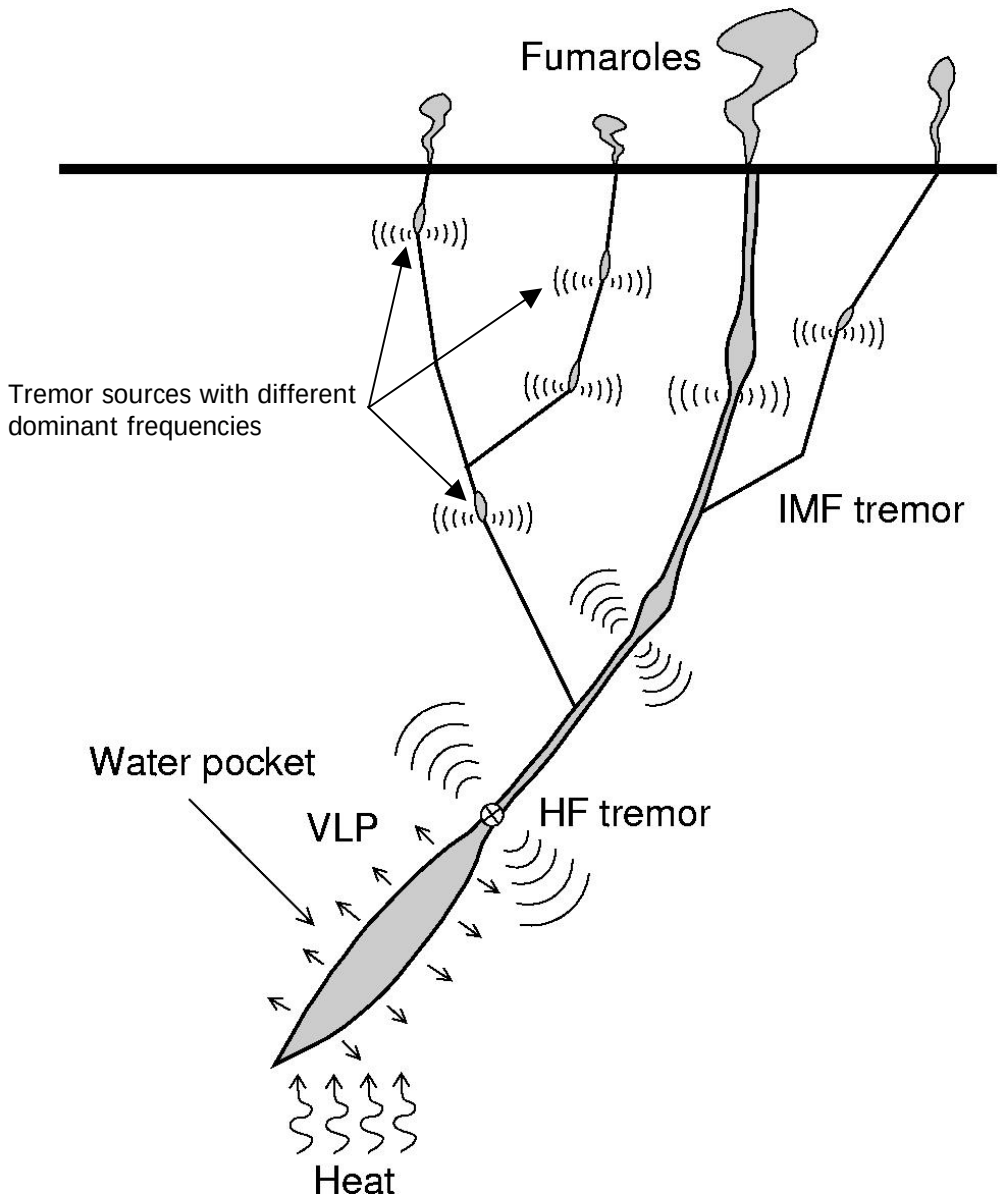
Fumaroles
Tremor sources with different dominant frequencies
IMF tremor
Water pocket
VLP
HF tremor
Heat

Fig.17

	Eigenvalues ($\times 10^{10}$Nm)		ϕ	θ
With topography	λ_1	5.9	32	12
	λ_2	3.7	−56	−7
	λ_3	2.9	−115	76
Without topography	λ_1	15.7	−2	1
	λ_2	9.1	147	89
	λ_3	3.4	88	−1

Table.1